

Seasonal contrast in the surface energy balance of the Sahel

R. L. Miller,^{1,2} A. Slingo,^{3,4} J. C. Barnard,⁵ and E. Kassianov⁵

Received 31 May 2008; revised 10 October 2008; accepted 29 December 2008; published 14 March 2009.

[1] Over much of the world, heating of the surface by sunlight is balanced predominately by evaporative cooling. However, at the Atmospheric Radiation Measurement (ARM) Mobile Facility (AMF) in Niamey, Niger, evaporation makes a significant contribution to the surface energy balance only at the height of the rainy season, when precipitation has replenished the reservoir of soil moisture. The AMF was placed at Niamey from late 2005 to early 2007 to provide measurements of surface fluxes in coordination with geostationary satellite retrievals of radiative fluxes at the top of the atmosphere, as part of the RADAGAST experiment to calculate atmospheric radiative divergence. We use observations at the mobile facility to investigate how the surface adjusts to radiative forcing throughout the year. The surface response to solar heating varies with changes in atmospheric water vapor associated with the seasonal reversal of the West African monsoon, which modulates the greenhouse effect and the ability of the surface to radiate thermal energy directly to space. During the dry season, sunlight is balanced mainly by longwave radiation and the turbulent flux of sensible heat. The ability of longwave radiation to cool the surface drops after the onset of southwesterly surface winds at Niamey, when moist, oceanic air flows onshore, increasing local column moisture and atmospheric opacity. Following the onset of southwesterly flow, evaporation remains limited by the supply of moisture from precipitation. By the height of the rainy season, however, sufficient precipitation has accumulated that evaporation is controlled by incident sunlight, and radiative forcing of the surface is balanced comparably by the latent, sensible, and longwave fluxes. Evaporation increases with the leaf area index, suggesting that plants are a significant source of atmospheric moisture and may tap moisture stored beneath the surface that accumulated during a previous rainy season. Surface radiative forcing during a dust aerosol outbreak is balanced comparably by net surface longwave and the sensible heat flux during the dry season, with the sensible flux increasing in importance with the onset of the summer monsoon winds. Measurements of surface fluxes by the AMF indicate broader features of the West African monsoon circulation and should be used to evaluate model simulations of the Sahel climate.

Citation: Miller, R. L., A. Slingo, J. C. Barnard, and E. Kassianov (2009), Seasonal contrast in the surface energy balance of the Sahel, *J. Geophys. Res.*, 114, D00E05, doi:10.1029/2008JD010521.

1. Introduction

[2] To maintain thermal equilibrium, Earth must balance absorbed solar radiation with an equal outward flux at thermal wavelengths. At the surface of the planet, however, solar heating is offset mainly through evaporation rather than thermal radiation. Over most regions, upward thermal radiation from the surface is trapped by greenhouse absorbers,

with the greatest trapping by water vapor and clouds, followed by gases like carbon dioxide [Kiehl and Trenberth, 1997]. Part of the absorbed flux is reradiated downward so that cooling of the surface by the net upward thermal flux is inefficient compared to evaporation [Raval and Ramanathan, 1989]. Surface evaporation is especially important within the tropical oceans [Liu *et al.*, 1994], and even over land where moisture is available from the soil reservoir.

[3] However, at the Atmospheric Radiation Measurement (ARM) Mobile Facility in Niamey, Niger, a semiarid region within the Sahel of western Africa, soil moisture is often so depleted that solar heating is balanced mainly by longwave radiation and the turbulent flux of sensible heat. Evaporation makes a significant contribution to the surface energy balance only near the height of the rainy season, when precipitation has replenished the soil reservoir. The circulation at Niamey exhibits a classic monsoonal pattern [Ramage, 1971; Webster, 1987], with a semiannual reversal of the

¹NASA Goddard Institute for Space Studies, New York, New York, USA.

²Also at Department of Applied Physics and Applied Math, Columbia University, New York, New York, USA.

³Environmental Systems Science Centre, University of Reading, Reading, UK.

⁴Deceased 14 October 2008.

⁵Pacific Northwest National Laboratory, Richland, Washington, USA.

prevailing surface wind between northeasterly during the Northern Hemisphere (NH) winter and southwesterly during the summer. Precipitation is confined to the summer season, when southwesterly flow brings moisture from the oceans and coastal vegetated regions. Growth of seasonal grasses and scattered clusters of trees within the savanna surrounding the ARM Mobile Facility is limited to the rainy season, despite nearly uniform temperatures throughout the year.

[4] At Niamey, the Sun is often partially obscured by aerosols, which are created by burning of vegetation, along with wind erosion of arid soils within the Sahel and Sahara [Slingo *et al.*, 2006; Johnson *et al.*, 2008]. Sunlight is reduced beneath the aerosol layer as a result of absorption and reflection back to space [Fouquart *et al.*, 1987a], while the aerosol layer emits longwave radiation back toward the surface [Guedalia *et al.*, 1984]. The climate response to aerosols depends upon which surface fluxes compensate the radiative perturbation, which generally reduces the net radiation into the surface [Miller and Tegen, 1998]. A reduction in the latent heat flux back into the atmosphere reduces precipitation globally [Coakley and Cess, 1985; Miller and Tegen, 1998], although radiative heating within the aerosol layer may induce ascent and cause a local increase in rainfall [Miller *et al.*, 2004b]. A reduction in the sensible heat flux decreases the vigor of boundary layer mixing. This reduces the magnitude of wind gusts associated with boundary layer eddies, along with the mixing of momentum down to the surface. Both effects reduce the surface wind speed, which impedes the lifting of additional soil particles into the atmosphere [Miller *et al.*, 2004a].

[5] Because of the large aerosol burden throughout the year, the Sahel is an ideal location to examine how the climate responds to aerosol radiative forcing at the surface. Measurements at the ARM Mobile Facility (AMF) at Niamey indicate that the surface energy fluxes respond to variations in atmospheric composition due to aerosols, clouds, and water vapor. The AMF is distinguished by its measurement of the entire suite of surface fluxes over a full seasonal cycle [Miller and Slingo, 2007]. The mobile facility was placed at Niamey from late 2005 to early 2007 to measure surface energy fluxes in coordination with retrievals of radiative fluxes at the top of the atmosphere by the Geostationary Earth Radiation Budget (GERB) instrument aboard the Meteosat-8 satellite. The measurements also overlapped with the African Monsoon Multidisciplinary Analyses (AMMA) experiment. Together, the surface and satellite measurements compose RADAGAST (Radiative Atmospheric Divergence using ARM Mobile Facility, GERB data, and AMMA Stations), which provided measurements of atmospheric radiative divergence with unusually high temporal resolution [Miller and Slingo, 2007; Slingo *et al.*, 2008].

[6] In this article, we use measurements at the ARM Mobile Facility during 2006 to examine how the surface energy fluxes compensate the seasonal cycle of solar heating, along with more rapid subseasonal fluctuations in surface radiative forcing due to variations in atmospheric constituents such as aerosols, clouds, and water vapor. In section 2, we describe the measurements used to characterize the seasonal cycle of the surface energy balance and atmospheric composition. In section 3, we show that sun-

light incident upon the surface is balanced differently according to the phase of the West African Monsoon. The cooling efficiency of net longwave radiation drops after the onset of the summer monsoon, when moist, oceanic air flows onshore, increasing local column moisture and atmospheric opacity at these wavelengths. During the summer monsoon, solar variations are balanced increasingly by turbulent fluxes, including evaporation. In section 4, we calculate the surface response to subseasonal fluctuations of surface radiative forcing due to changes in atmospheric composition. The importance of the turbulent fluxes depends upon the availability of soil moisture and the ability of the forcing to change the strength of mixing within the planetary boundary layer. In section 5, we consider the implications of the AMF measurements for seasonal forecasting and evaluation of simulations of the West African monsoon by climate models. Our conclusions are given in section 6.

2. Measurements

[7] The ARM Mobile Facility was deployed at the airport in Niamey, Niger (2.18°E, 13.48°N) between November 2005 and January 2007. The instruments measuring surface fluxes were located in an open field composed of annual grasses punctuated by clusters of trees. Figure 1, a photo taken in late August 2006, near the end of the rainy season, shows expansive patches of green grass roughly a meter high surrounding the instruments. In contrast, a photograph from November 2005 at the beginning of the dry season [Miller and Slingo, 2007, Figure 5b] shows grasses that have withered and receded, exposing large expanses of bare reddish soil around the instruments, only a few months after an unusually rainy summer [Slingo *et al.*, 2008]. The instruments measuring surface turbulent and radiative fluxes were situated roughly 80 meters from the main instrument trailer and airport buildings to the south and southeast. These structures were within the estimated 200 meter fetch of the turbulent flux instruments, and had the potential to influence the measured fluxes [Cook and Pekour, 2008]. However, because of the persistent monsoonal flow, the buildings were rarely upwind. Between June and September 2006, when the surface winds were typically from the southwest, the average wind direction measured every 30 min by the eddy correlation instrument (described below) was between the south and east only 8% of the time. The surface winds originated from this quadrant only 10% of the time during the months of 2006 corresponding to the dry season, when northeasterly flow was more typical. The flux instruments were downwind of a small grove of trees roughly a hundred meters to the west and southwest. These trees were often upwind of the instruments during the rainy season, and their transpiration along with that of the surrounding grass combined to influence the measured fluxes. The seasonal change in vegetation altered solar heating of the surface through the ground albedo, which was as bright as 0.25 during the dry season but darkened to 0.20 by the end of the rainy season [McFarlane *et al.*, 2009]. A complete list of the instrumentation at the ARM Mobile Facility is given by Miller and Slingo [2007]. Here we describe the instruments that provide data analyzed in this study, listed in Table 1.



Figure 1. Turbulent and radiative flux instruments at the ARM Mobile Facility at the Niamey airport on 30 August 2006 near the end of the rainy season. For comparison, Figure 5b from *Miller and Slingo* [2007] shows the site in November 2005 at the beginning of the dry season (and identifies individual instruments). Photo by Mike Alsop, provided courtesy of the U.S. Department of Energy's Atmospheric Radiation Measurement Program.

[8] The surface energy budget consists of turbulent and radiative fluxes. Turbulent fluxes of latent and sensible heat were calculated using an eddy correlation instrument, which computes means and covariances of wind speed, tempera-

ture, and water vapor measured over a 30 min period. Values of the specific heat of air at constant pressure C_p and the latent heat of vaporization L_v , calculated using temperature and humidity measured by the instrument and used to convert measured covariances into heat fluxes, were also archived every 30 min. Instrumental uncertainty is estimated at less than 5% and 6% for the sensible and latent heat fluxes, respectively [Cook and Pekour, 2008], corresponding to errors of less than 5 W m^{-2} for daily averages.

[9] Downwelling shortwave and longwave radiation were measured every minute by broadband radiometers. Upwelling fluxes were measured 2 m above the surface with the same temporal frequency. *Slingo et al.* [2006] estimate instrumental uncertainty of the instantaneous fluxes at less than 10 W m^{-2} for shortwave and just over 5 W m^{-2} for longwave, although these can be larger when diffuse scattering is elevated as during an aerosol outbreak. The downwelling longwave flux was measured independently by a second instrument, and the difference provides another measure of the uncertainty of each estimate. Over the fourteen months of the experiment, the root-mean-square difference was 3.6 W m^{-2} , which was largest typically during midmorning and midafternoon. The root-mean-square difference of the diurnal cycle was 0.8 W m^{-2} . These are small compared to the anomalies of daily averaged downwelling longwave, which are typically a few tens of W m^{-2} during the dry season (November to April).

[10] The net (or total) flux of heat into the surface departs from zero when averaged over a year, even if storage by the

Table 1. Summary of Analyzed Measurements

Measured Quantity	Data Stream ^a	Variable Name ^b	Dates Available	Resolution
<i>Broadband Radiative Fluxes</i>				
Downwelling shortwave	skyrad60s	down_short_hemisp	26 Nov 2005 to 7 Jan 2007	1 min
Downwelling longwave	skyrad60s	down_long_hemisp_shaded1	26 Nov 2005 to 7 Jan 2007	1 min
Upwelling shortwave	gndrad60s	up_short_hemisp	24 Nov 2005 to 7 Jan 2007	1 min
Upwelling longwave	gndrad60s	up_long_hemisp	24 Nov 2005 to 7 Jan 2007	1 min
<i>Turbulent Fluxes</i>				
Latent heat flux	30ecor	lv_e	26 Nov 2005 to 7 Jan 2007	30 min
Sensible heat flux	30ecor	h	26 Nov 2005 to 7 Jan 2007	30 min
<i>Atmospheric Opacity</i>				
Column water vapor	sondewnpn	dp	7 Jan 2006 to 7 Jan 2007	6 h
MFRSR AOT ^c	-	-	25 Nov 2005 to 7 Jan 2007	20 s
ISCCP DX COT ^d	-	-	1 Nov 2005 to 31 Dec 2006	3 h
<i>Meteorological Quantities</i>				
Rainfall	met	precip_rate_mean	6 Jan 2006 to 7 Jan 2007	1 min
Surface specific humidity q_s	30ecor	mr	26 Nov 2005 to 7 Jan 2007	30 min
Surface air temperature T_s	30ecor	mean_t	26 Nov 2005 to 7 Jan 2007	30 min
<i>Thermodynamic Quantities</i>				
C_p ^e	30ecor	cp	26 Nov 2005 to 7 Jan 2007	30 min
L_v ^f	30ecor	lv	26 Nov 2005 to 7 Jan 2007	30 min
<i>Environmental Quantities</i>				
MODIS LAI ^g	-	-	31 Oct 2005 to 1 Jan 2007	8 days

^aName of the data stream at the ARM data archive: <http://www.archive.arm.gov>.

^bNetcdf name of the variable in the daily data stream file.

^cMultifilter Rotating Shadowband Radiometer aerosol optical thickness.

^dInternational Satellite Cloud Climatology Project cloud optical thickness. DX denotes retrievals within a pixel of roughly 30 km on a side.

^eSpecific heat of moist air at constant pressure.

^fLatent heat of vaporization.

^gModerate Resolution Imaging Spectroradiometer leaf area index.

ground is neglected, because of biases in the individual instruments that measure the turbulent and radiative fluxes. As one measure of the precision with which the surface energy balance can be defined, the net heat flux at the surface and its average imbalance over the course of the campaign were computed by summing the net solar and longwave fluxes together with the turbulent fluxes. To be consistent with the temporal resolution of the turbulent fluxes, the radiative fluxes were resampled every 30 min (after filtering periods shorter than 60 min to reduce aliasing). The net heat flux was computed at times when all of the separate turbulent and radiative fluxes were available, which during 2006 resulted in values for roughly 350 days, depending upon the time of day. The average imbalance of the net heat flux during 2006 was -6.5 W m^{-2} . This value reflects measurement error (along with possible interannual variations in heat storage), but also the fact that slightly more observations were available during the early afternoon (when the heating of the ground was largest) than around sunrise. If we form the average imbalance by averaging over the mean diurnal cycle (so that each time of day is equally represented), the average imbalance increases slightly to -6.6 W m^{-2} . Either way, this imbalance is small compared to daily fluctuations in the individual turbulent and net solar and longwave fluxes, which are on the order of a few tens of W m^{-2} .

[11] In section 4, we interpret variations in the surface radiative fluxes in terms of changes in atmospheric opacity related to water vapor, aerosol load, and cloud cover. Water vapor within the atmospheric column was provided by Vaisalla RS-92 radiosondes. The sondes were launched four times daily at times clustered around 0530, 1100, 1730, and 2300 local standard time. The column water was determined by summing over the depth of the sonde path, resulting in monthly averaged values that are comparable to those retrieved by the NASA Water Vapor Project (NVAP [Simpson *et al.*, 2001]). Good correspondence in daily fluctuations of column water vapor are found with respect to Microwave Radiometer retrievals, especially during the dry season [Slingo *et al.*, 2008]. Column water vapor corresponding to individual sondes has a typical dry bias of less than 5% around noon, and a smaller wet bias at night compared to values derived from the Global Positioning System [Bock *et al.*, 2008]. These differences are small compared to daily averaged anomalies.

[12] Aerosol optical thickness (AOT) was retrieved from measurements of the direct solar flux at six wavelengths by the Multifilter Rotating Shadowband Radiometer (MFRSR [Harrison *et al.*, 1994; McFarlane *et al.*, 2009]). Measurements were taken every 20 s during daylight hours, and interpolation was used when the presence of clouds precluded the retrieval of AOT. To interpret daily variations in the surface radiative fluxes during the dry season (section 4), we form daily averages of the MFRSR retrieval of AOT at 500 nm. Without interpolation, clouds prevent the retrieval of AOT and the construction of a daily average roughly 3 days a month during the dry season, and on 8 days between 27 January and 18 February. Of the remaining days, daily averages are occasionally constructed from only a small number of retrievals, which increases the sampling uncertainty. However, we found that daily averages of AOT retrieved from the MFRSR at the mobile facility in Niamey

are highly correlated with the 440 nm AOT retrieved at the AERONET site at Banizoumbou, 50 km to the northeast. Correlations within a 15-day moving window are typically between 0.9 and 1.0 during the dry season, except during early February, when MFRSR retrievals of AOT are precluded by clouds on many days and the correlation falls to roughly 0.8. The high correlation suggests that aerosol variations occur over a broad spatial scale, encompassing both instrument sites, and that the MFRSR retrievals give a reliable estimate of daily averaged AOT, despite our interpolation and large day-to-day variations in the number of available retrievals.

[13] Cloud optical thickness is retrieved by the International Satellite Cloud Climatology Project (ISCCP [Rossow and Duenas, 2004]), using visible radiances measured by Meteosat every 3 h. On 1 July 2006, midway through the AMF campaign at Niamey, the platform carrying the radiance instrument changed from Meteosat-7 to Meteosat-8. We formed a daily average of cloud optical thickness by combining retrievals for the 30 km pixel encompassing Niamey at 0900, 1200, and 1500 local time. (Retrievals are not made at 0600 and 1800 local time because of the low solar zenith angle.) Missing retrievals preclude the calculation of a daily average about 3 days a month. The algorithm used to retrieve of cloud optical thickness depends upon whether a water or ice cloud is detected, which is determined mainly by cloud top temperature.

[14] Seasonal variations in measured evaporation are interpreted in terms of soil moisture, whose variation is inferred from the seasonal cycles of accumulated precipitation and vegetation upwind of the instrument. Precipitation is measured using an optical instrument on a 10 m tower at the mobile facility. The instrument continuously measures the interruption of an infrared beam by rainfall, archiving the total every minute. Precipitation was also measured using a conventional rain gauge roughly a kilometer away at another site within the Niamey airport (H. Hama, personal communication, 2008). During 2006, the AMF optical instrument recorded 37.6 cm of rainfall compared to 42.4 cm by the gauge [Slingo *et al.*, 2008]. The AMF values are generally smaller compared to the gauge values, and the near agreement of the annual totals is due to a single 20 min event on the morning of 24 July, when 9.4 cm was recorded by the AMF instrument. No other measurement corroborates the occurrence of rainfall at this time. Meteosat visible images show only broken clouds, while no rain is indicated by either the airport gauge or 3-hourly rainfall retrievals calculated from a blend of Tropical Rainfall Measuring Mission (TRMM) radar and microwave measurements along with outgoing longwave radiances (3B42 Version 6 [Huffman *et al.* 1997]). As a result, we exclude this value from our analysis in subsequent sections. Measurement of rainfall by the AMF optical gauge was complicated by the persistent aerosol haze at Niamey, which necessitated the replacement of the original instrument during the middle of May 2006. Despite disagreement about a few specific events, the AMF optical instrument and airport rain gauge generally noted the occurrence of precipitation consistently. Out of the roughly 180-day rainy season at Niamey, 52 days were identified as rainy by the AMF instrument compared to 57 days for the gauge (with a rainy day defined by an accumulation of at least 0.1 mm of rain), with 39 of these

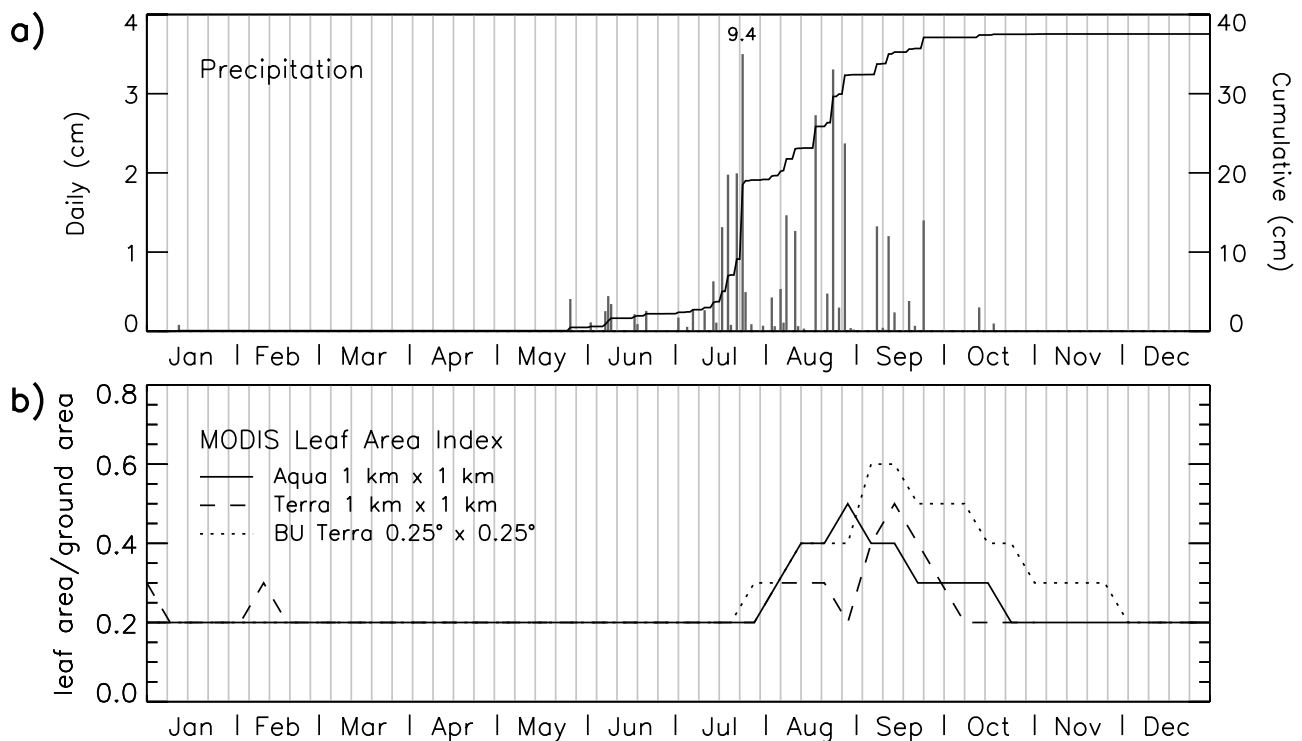


Figure 2. (a) Daily (gray) and cumulative (black) rainfall in cm, measured by the optical instrument at the ARM Mobile Facility in Niamey, Niger. Daily rainfall measured on 24 July 2006 was off the scale at 9.4 cm, although this rain event was not corroborated by other data sets. Rainfall was not measured between 13 May and 26 May, when the original instrument was replaced, but no rainfall was recorded during this time at another site in Niamey (*Slingo et al.*, 2008). (b) Leaf area index at Niamey retrieved by the MODIS Terra and Aqua instruments at 1 km resolution, as well as a Boston University product gridded at 0.25° longitude by 0.25° latitude. Light gray vertical lines in Figure 2 and subsequently in Figures 3–6 and 8–10 are spaced 7 days apart, beginning on 1 January 2006.

days in common. The overlap increases to roughly 45 days, if events around midnight are included that were attributed to different days by the two instruments (K. Kehoe, personal communication, 2008). For comparison, only 10 to 25 days would be in common if either instrument were identifying rainy days at random, suggesting the general concurrence of the two instruments (see Appendix A). The AMF instrument is in better agreement than the gauge with respect to the 3-hourly TRMM retrievals, according to a rank correlation test. However, this may simply indicate that the AMF and satellite instruments retrieve rainfall using variables that are highly correlated, and may not indicate increased reliability of the AMF instrument relative to the gauge. Both the optical instrument and gauge indicate similar seasonal accumulation of rainfall during 2006, with a regular succession of precipitation events delayed until the middle of July (Figure 2a) [*Slingo et al.*, 2008].

[15] We characterize seasonal variations in vegetation near the instrument site using the leaf area index (LAI), defined as green leaf area per unit ground area and retrieved by the Moderate Resolution Imaging Spectroradiometer (MODIS) instrument on the Terra and Aqua satellites [*Yang et al.*, 2006a]. The LAI is retrieved as part of a radiative transfer calculation. When the surface is repeatedly obscured by clouds, a less accurate value is provided on the basis of an empirical relation to the retrieved Normalized Difference Vegetation Index, although this was never necessary at

Niamey during the AMF deployment. The MODIS product represents the largest of the LAI values retrieved during each successive 8-day period, a duration chosen to allow high temporal resolution while reducing contamination of the LAI by undetected clouds and aerosols, which otherwise spuriously reduce the retrieved value [*Yang et al.*, 2006a]. We use the LAI product from Collection 5, available within a 1 km by 1 km grid. The LAI is archived in increments of 0.1, which at Niamey is larger than the 12% retrieval uncertainty estimated by *Yang et al.* [2006b]. For comparison of vegetation at the AMF site to a larger area, we also use a gridded product formed from Terra LAI retrievals averaged over an area of 0.25° longitude by 0.25° latitude, made available by Boston University. The three retrievals show a similar seasonal cycle, with the LAI rising above the dry season value only after the middle of July following the resumption of frequent rain events (Figure 2b). The outlier is the Terra 1 km retrieval, whose temporary return to the dry season value at the end of August is contradicted by the seasonal vegetation at the AMF photographed in Figure 1. It is possible that undetected clouds are influencing the Terra retrieval for this single date. In subsequent discussions of the LAI, we will emphasize the Aqua 1 km and Boston University 0.25° gridded products.

[16] With the exception of the MFRSR aerosol optical thickness, where we interpolate to fill missing values, we

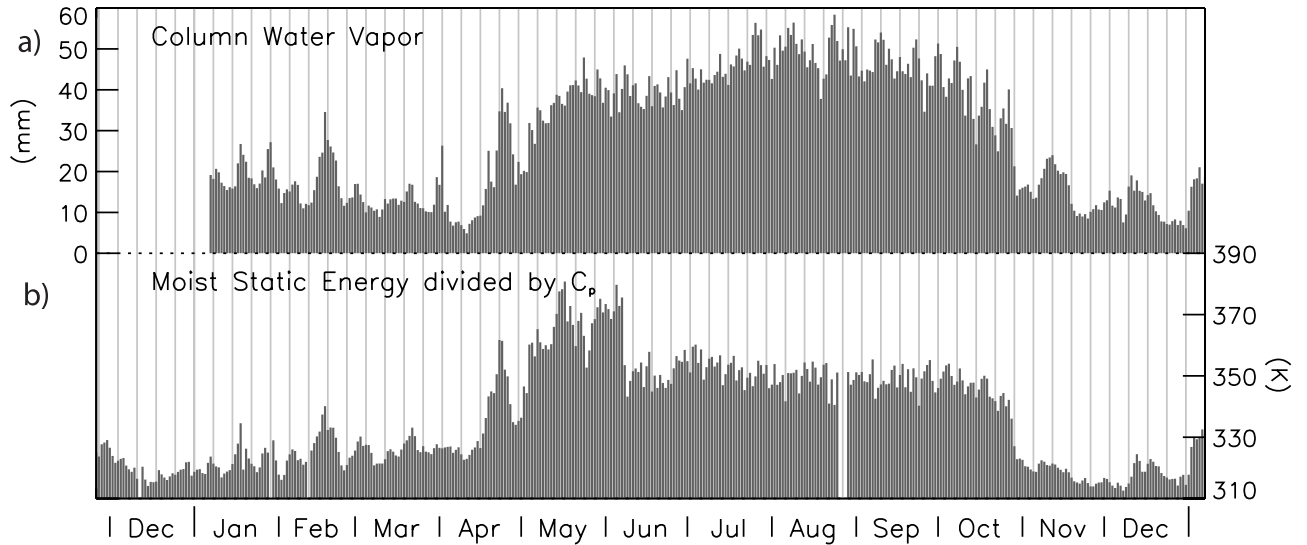


Figure 3. (a) Column-integrated radiosonde water vapor (mm) and (b) moist static energy (divided by C_p to have units of K) measured at the ARM Mobile Facility at Niamey, Niger.

exclude periods with missing measurements from our analysis.

3. Seasonal Cycle of the Surface Energy Balance

3.1. Measurements at the AMF

[17] In this section, we describe the seasonal evolution of the surface energy balance in the context of the regional climate. A more extensive description of the climate and atmospheric variability measured during the deployment of the ARM Mobile Facility in 2006 is provided by *Slingo et al.* [2008].

[18] At Niamey, the surface winds divide the year into two seasons, indicating a monsoon circulation [*Nicholson and Grist*, 2003]. During the dry season, between November and April, the northeasterly Harmattan wind brings

desert air to Niamey that eventually flows offshore toward the Atlantic Intertropical Convergence Zone. Then, within a few-week period beginning in April, the surface wind reverses with the arrival of the summer phase of the West African monsoon. Until late October, there is comparatively weak southwesterly flow bringing moist air from the Gulf of Guinea. The seasonal reversal of the circulation during the 2006 deployment of the AMF is illustrated by back trajectories of air arriving at Niamey [*Slingo et al.*, 2008].

[19] The monsoonal reversal of the surface wind in late April 2006 at Niamey is marked by an abrupt increase in column water vapor, measured from the four times daily radiosondes and integrated with respect to height, shown in Figure 3. Surface measurements of temperature T_s and specific humidity q_s indicate an abrupt and coincident increase in moist static energy (equal to $h = C_p T_s + L_v q_s$

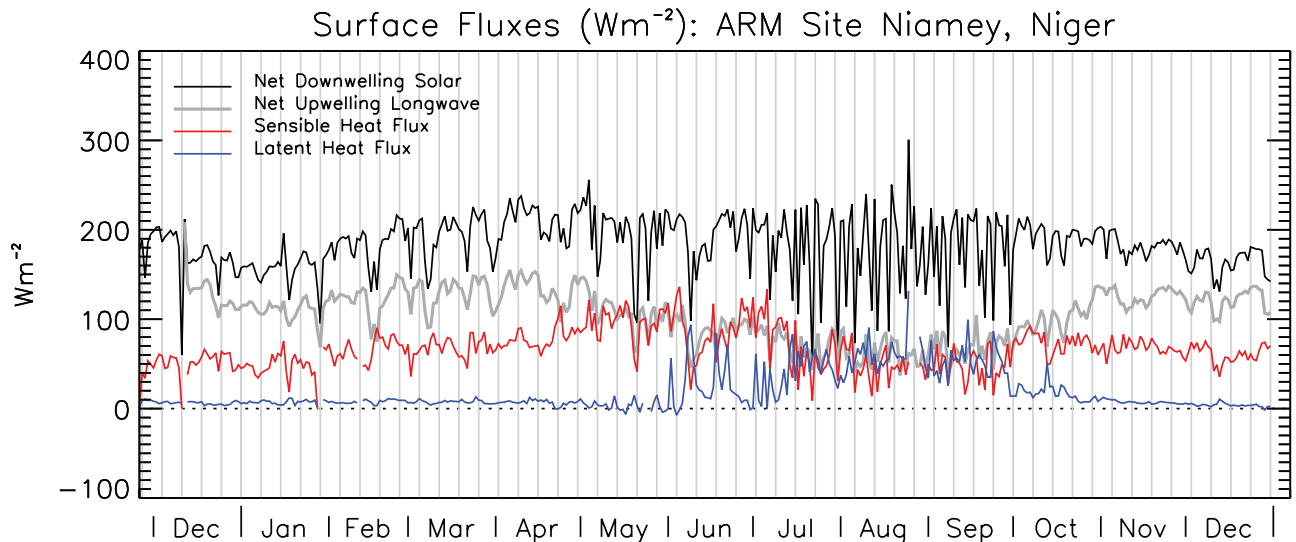


Figure 4. Daily averaged surface fluxes ($W m^{-2}$) measured at the ARM Mobile Facility at Niamey, Niger.

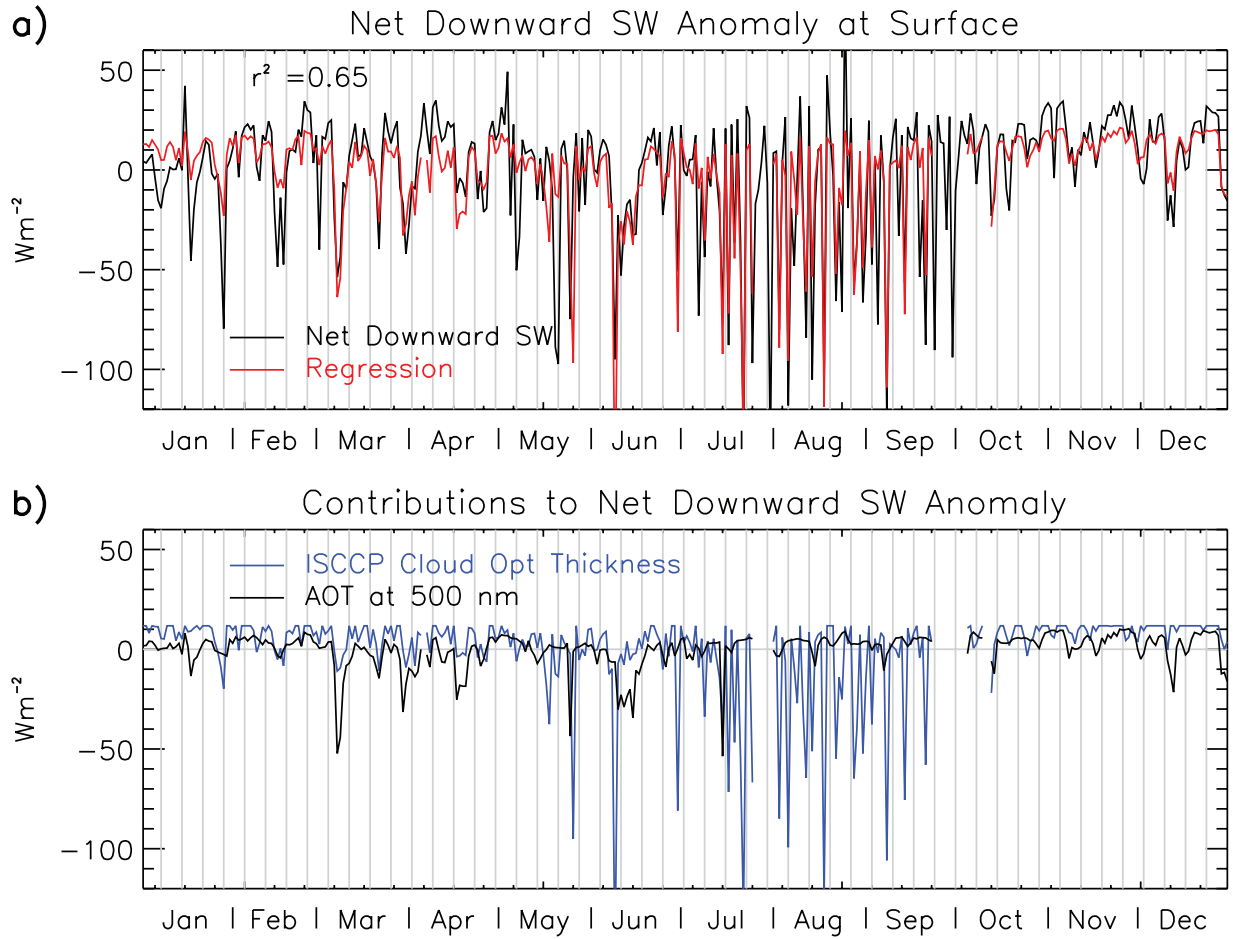


Figure 5. (a) Daily averaged anomalous net downward flux of solar radiation at the surface $R'_{SW}(0)$ defined in section 4.1 and measured at the ARM Mobile Facility at Niamey, Niger (black, $W m^{-2}$), versus the downward flux $\hat{R}'_{SW}(0)$ constructed by multiple regression with respect to ISCCP cloud optical thickness τ'_C and aerosol optical thickness τ'_A (red). The regression model $\hat{R}'_{SW}(0) = (-4.52 \pm 0.39) \tau'_C + (-24.3 \pm 5.4) \tau'_A$ represents 65% of the measured variation of the daily downward flux. The uncertainty range for each regression coefficient is calculated using a two-sided test at the 95% confidence level. (b) Contributions to the net downward solar anomaly at the surface ($W m^{-2}$) by clouds (blue) and aerosol optical thickness (black) according to the regression model.

where each quantity is based upon measurements by the eddy correlation instrument). High moist static energy at the surface indicates unstable air prone to convective ascent and precipitation [Emanuel, 1994]. At the latitude of Niamey, climatological precipitation increases steadily between April and early August [Nicholson and Grist, 2003]. During 2006, the winds reversed on schedule in late April [Slingo *et al.*, 2008]. However, despite substantially increased values of moist static energy and column moisture, rainfall remained sporadic and modest for over two months until the middle of July (Figure 2a). Vegetation around the AMF reemerged with the accumulation of rainfall. Figure 2b shows that the leaf area index rose above its dry season value only after mid-July when rainfall began to arrive regularly. The LAI continued to increase past late August, when the instruments were photographed in Figure 1. When rainfall became infrequent after the middle of September, the LAI began its decline, and returned to its dry season value by the end of November. Vegetation declined more rapidly at the airport site containing the AMF instruments,

compared to the wider area sampled by the Boston University 0.25° product. Total rainfall was below normal during the AMF deployment in 2006, following anomalously high rainfall during the preceding year [Slingo *et al.*, 2008].

[20] The increase of column moisture with the arrival of the southwesterly wind alters the surface energy budget. The radiative and turbulent surface fluxes, along with their seasonal variation during the measurement campaign, are shown in Figure 4. Solar radiation at the top of the atmosphere (TOA) varies in part with the seasonal evolution of the solar zenith angle. This angle is greatest in late April and August when the Sun passes overhead, but the daily averaged TOA flux peaks later in the year because the day lengthens toward the summer solstice [e.g., Hartman, 1994]. Solar radiation also varies inversely with the Earth-Sun distance, which is greatest in July. When the effects of the zenith angle, length of day, and Earth-Sun distance are taken together, the daily average of the TOA incident solar flux peaks in early May and is fairly steady until August. This seasonal variation at TOA is exhibited by the net

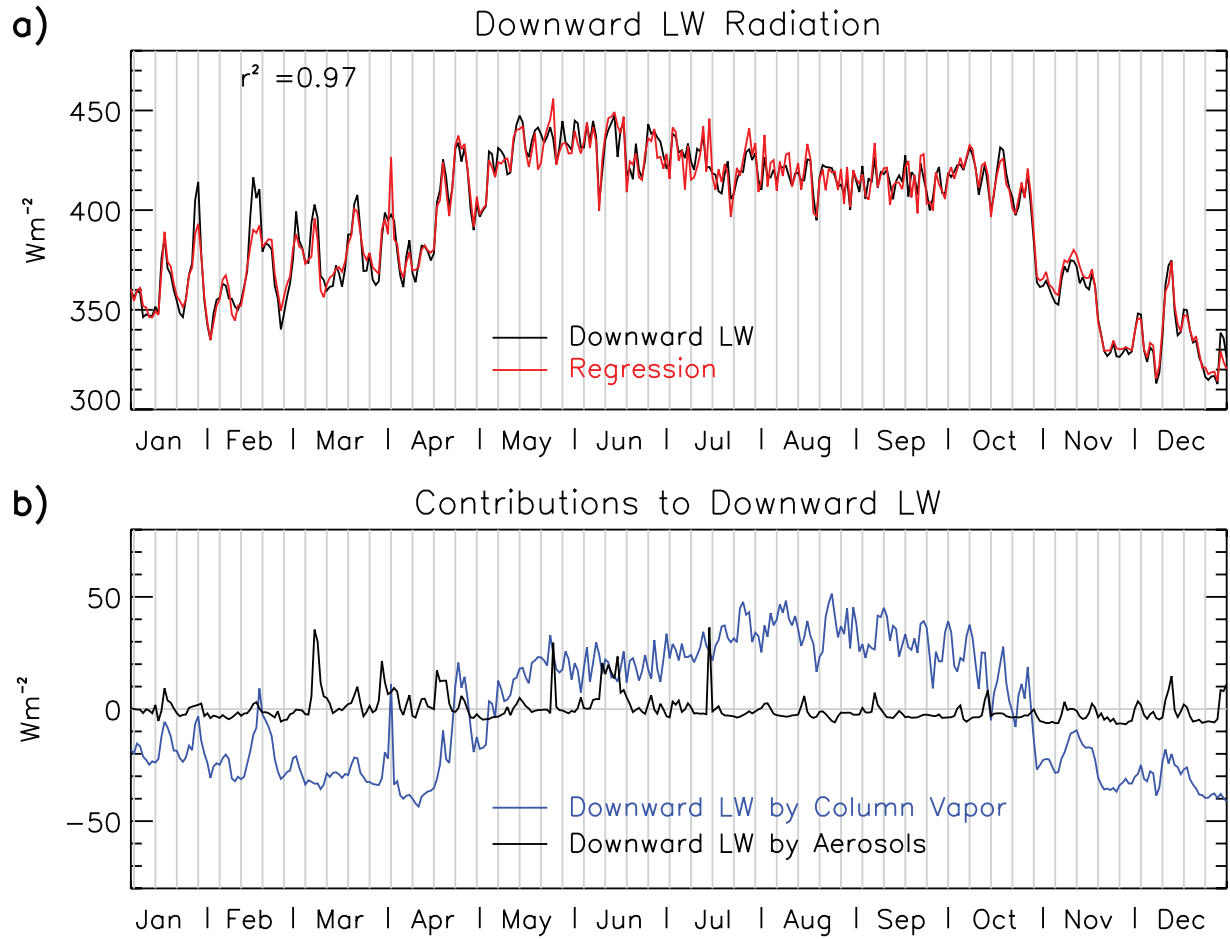


Figure 6. (a) Daily averaged downward flux of longwave radiation at the surface $R'_{LW\downarrow}(0)$ measured at the ARM Mobile Facility (black, W m^{-2}), versus the downward flux $\hat{R}'_{LW\downarrow}(0)$ constructed by multiple regression with respect to surface air temperature T'_s , column water vapor q' , and aerosol optical thickness τ'_A (red). The regression model $\hat{R}'_{LW\downarrow}(0) = (4.84 \pm 0.20) T'_s + (1.78 \pm 0.042) q' + (16.5 \pm 1.83) \tau'_A$ represents 97% of the measured variation of the daily downward flux. The uncertainty range for each regression coefficient is calculated using a two-sided test at the 95% confidence level. (b) Contributions to downward longwave at the surface (W m^{-2}) by water vapor (blue) and aerosol optical thickness (black) according to the regression model.

downwelling solar flux at the surface (equal to the measured difference of the downwelling and upwelling solar fluxes), plotted in Figure 4.

[21] Solar heating of the surface also varies as a result of seasonal changes in clouds and aerosols. Solar radiation transmitted to the surface is reduced to the greatest extent by clouds during the rainy season. This is illustrated in Figure 5b, which shows the approximate reduction in the net surface solar flux by clouds as inferred from a simple regression model described in the next section. During 2006, the correlation between cloud optical thickness and the surface solar anomaly in Figure 5a is -0.76 . Cloud attenuation of sunlight is largest during the rainy season, when it typically peaks every few days (as shown in the next section), corresponding to the passage of deep convective clouds within African waves [Burpee, 1972]. Over the entire year, aerosols have a smaller effect than clouds upon the surface solar flux, although Figure 5b shows that solar heating of the surface was reduced by a few tens of

W m^{-2} during a dust outbreak in early March 2006 [Slingo *et al.*, 2006; McFarlane *et al.*, 2009]. Figure 5b shows that aerosols reduced the net solar flux by this order, during several other dust outbreaks between March and June of 2006.

[22] During the dry season, solar heating is balanced largely by the net flux of upward longwave radiation from the surface (equal to the measured difference of the upwelling and downwelling longwave fluxes). Column moisture over the Sahel is small compared to values in neighboring regions of tropical convection [Randel *et al.*, 1996], and as a result of the weak greenhouse effect, the surface can cool efficiently by radiating longwave. Slingo *et al.* [2009] divide the outgoing longwave radiation (OLR), measured with the Geostationary Earth Radiation Budget instrument on Meteosat-8, by upwelling longwave at the surface calculated from surface air temperature. This fractional index increases as the greenhouse effect weakens, and the index is largest during the dry season, consistent with

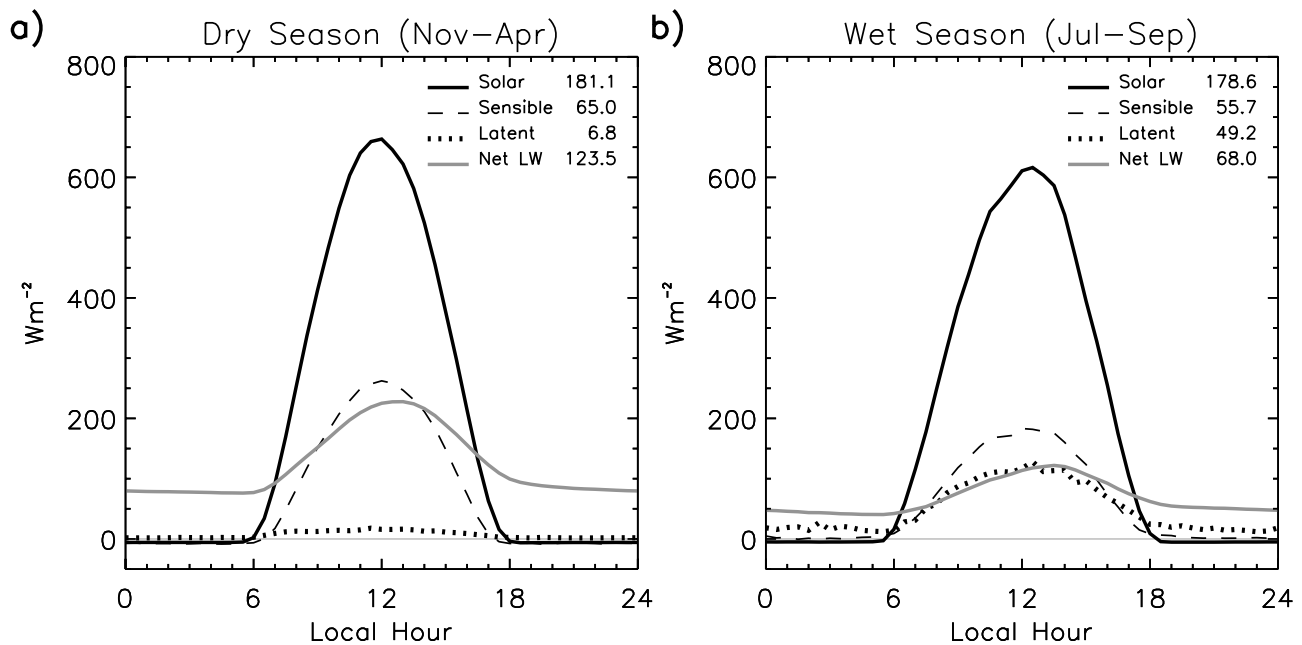


Figure 7. Diurnal cycle of surface fluxes (W m^{-2}) during (a) the dry season (November–April) and (b) the height of the wet season (July–September), measured at the ARM Mobile Facility at Niamey, Niger. Diurnal averages of each flux are listed at the top right corner. Radiative fluxes were subsampled every 30 min (after filtering periods shorter than 60 min to reduce aliasing) to be consistent with the resolution of the turbulent fluxes.

greater OLR originating from the surface. During the dry season, the turbulent flux of sensible heat is roughly half the longwave, while the flux of latent heat is effectively zero, implying that any moisture remaining in the soil since the anomalously large rainfall in the year prior to the installation of the AMF is too deep to be tapped by evaporation.

[23] With the arrival of moist air in late April, the downward flux of longwave emitted by the atmosphere increases markedly (Figure 6). Using a radiative transfer model, *Bharmal et al.* [2009] show that the downward longwave increase is consistent with the observed threefold increase in column moisture. Consequently, cooling of the surface by longwave emission becomes less efficient, and the net upward longwave flux at the surface falls to the level of the sensible heat flux (Figure 4). Evaporation increases as precipitation replenishes the reservoir of soil moisture, and by late July the longwave, sensible, and latent heat fluxes are of comparable importance. Aside from a few episodes in June following clusters of rainy days, the increase in evaporation coincides with the growth of vegetation (indicated by the leaf area index in Figure 2b), whose roots tap moisture below the soil surface. Evaporation falls off quickly after the decline of the LAI and the end of the rains in the middle of September. When the monsoon winds reverse in late October, indicated by a drop in moist static energy and column moisture (Figure 3), longwave radiation is reestablished as the predominant mechanism balancing absorbed sunlight.

[24] In summary, the surface energy balance can be characterized by three distinct periods. During the dry season, greenhouse absorption by water vapor is smallest, and the surface cools efficiently by radiating directly to

space. The second period follows the return of moist air associated with the summer monsoon, which makes the column comparatively opaque to longwave radiated by the surface, and the sensible heat flux increases to compensate. Finally, after the summer rains replenish the reservoir of soil moisture, the latent heat flux becomes of comparable importance.

[25] The contrast between the diurnal cycle of the surface energy balance during the dry season and the height of the rainy season, when soil moisture is sufficient to sustain evaporation, is shown in Figure 7. Throughout the year, the sensible heat flux at midday represents the largest instantaneous flux of heat from the surface into the atmosphere. However, net upward longwave remains positive at night despite its reduced amplitude, accounting for its predominant total contribution to the surface energy balance during the dry season.

[26] Figure 7 shows that the longwave flux peaks slightly later in the day than the sensible heat flux. The sensible heat flux is related to the difference of the ground and surface air temperatures multiplied by a bulk coefficient that depends upon wind speed and atmospheric stability [*Arya*, 2001], as described in greater detail in the next section. Both the temperature difference and bulk coefficient peak just before noon, accounting for the midday maximum of the sensible heat flux. In contrast, net upward longwave depends upon the ground temperature, which is highest slightly after noon, and downwelling longwave emitted by the atmosphere. The latter depends upon air temperature and moisture. The surface mixing ratio measured by the eddy correlation instrument decreases by about ten percent between sunrise and midafternoon, presumably because of the expansion of the boundary layer and the entrainment of dry air. The

moisture decrease offsets the effect of increasing air temperature upon the downwelling longwave. Because of this offset and the smaller diurnal cycle of atmospheric temperature compared to the ground, the diurnal cycle of net longwave approximately follows the upward flux which peaks just after noon.

3.2. Comparison to Previous Campaigns

[27] Surface fluxes within the Sahel have been measured by previous campaigns. One of the earliest was ECLATS (Etude de la Couche Limite Atmosphérique Tropical Sèche) between November and December 1980 at the start of the dry season [Fouquart *et al.*, 1987b]. Surface fluxes of solar and longwave radiation along with heat flux into the soil were measured at the Niamey airport near the future AMF site. The sensible heat flux was determined from measurements of temperature and wind speed using a bulk formula, with the latent heat flux determined as a residual. Measurements of these fluxes were subsequently made during the transition into the rainy season in the final weeks of April 1984 at Yantala, Niger, a few kilometers northwest of Niamey [Pagès *et al.*, 1988]. Both experiments showed that solar heating of the surface was balanced primarily by longwave emission and the sensible heat flux, with evaporation only a small residual [Frangi *et al.*, 1992]. This is consistent with the AMF measurements described here, where the latent heat flux makes a significant contribution to the total surface flux only at the height of the rainy season.

[28] Because of large spatial variations in rainfall that increase with distance from the Sahara, the Sahel is a heterogeneous land surface with a wide range of plant species and environments beyond the savanna that characterizes the AMF site. To account for the effect of this heterogeneity on the surface energy balance, surface fluxes have been measured over a variety of vegetation types. The restriction of significant evaporation until midsummer was found in measurements by an eddy correlation instrument located over a millet field at Sadoré, about 45 km south of Niamey, during the 1985 through 1988 growing seasons [Gash *et al.*, 1991; Wallace *et al.*, 1993]. This restriction was also shown in episodic measurements of evaporation within savanna and dense shrubland (“tiger bush”) during the Sahelian Energy Balance Experiment (SEBEX) between the summers of 1989 and 1990 [Verhoef *et al.*, 1999], and during the latter half of the 1992 rainy season within the Intensive Observing Period of the Hydrologic-Atmospheric Pilot Experiment in the Sahel (HAPEX-Sahel [Gash *et al.*, 1997]). Consistent with the AMF measurements, these campaigns found that evaporation becomes significant only after the resumption of regular rain events at measurement sites ranging from the savanna that characterizes the AMF, to shrubland and cultivated millet.

4. Surface Response to Subseasonal Variations in Atmospheric Constituents

[29] Sunlight incident upon the surface varies with the slow, seasonal change of the solar zenith angle, but also as a result of fluctuations in atmospheric opacity due to clouds, water vapor, and aerosols, for example. These constituents shield the surface from solar radiation through reflection

and absorption, while trapping longwave radiation and reemitting it toward the surface [Ramanathan *et al.*, 1989; Claquin *et al.*, 1998]. During one particularly strong dust outbreak over the AMF at Niamey during March 2006, the midday solar flux was reduced by 250 W m^{-2} while downward atmospheric emission of longwave into the surface increased by 50 W m^{-2} [Slingo *et al.*, 2006]. In this section, we calculate the surface response to radiative forcing associated with subseasonal variations in atmospheric constituents, and compare the ability of the turbulent fluxes and longwave emission to regulate the temperature of the surface.

4.1. Calculation of Subseasonal Variations of Surface Radiative Forcing

[30] We calculate the surface radiative forcing by combining the net downwelling solar flux with the component of the downwelling longwave flux that is related to changes in atmospheric composition. In a model, it is straightforward to calculate forcing by simply contrasting the radiative fluxes computed in the presence and absence of some constituent, while holding climate variables such as temperature fixed. Calculating the forcing from an observed atmospheric profile is complicated because the observed temperature responds to the forcing. Because longwave emission depends upon temperature, the measured longwave flux will indicate not merely the forcing but also part of the response. We need to distinguish the contribution to the measured downwelling longwave by a change in composition from the longwave contribution due to the response of the column temperature to the forcing.

[31] Consider for example, an increase in aerosol optical thickness resulting from the passage of a dust plume. Absorption of radiation within the aerosol layer reduces the downwelling solar flux impinging on the surface, while increasing the downwelling flux of longwave [Slingo *et al.*, 2006]. The downwelling longwave measured at the surface changes with the increase in atmospheric opacity and emission by the dust layer, but also with changes in the atmospheric emitting temperature. The forcing is the reduction of net solar radiation into the surface, offset by the increase in downwelling longwave due to the increase in opacity and emission, while the change in downwelling longwave due to the perturbed temperature is a response to the forcing. Thus, in order to infer the surface response to fluctuations in aerosol (or more generally to variations in atmospheric composition), we need to distinguish the contributions to the measured downward longwave by the forcing and the temperature response.

[32] To separate the forcing and response contributions to the observed downward longwave flux, we regress this flux against surface air temperature and atmospheric constituents such as water vapor and aerosols. Then:

$$\hat{R}'_{LW\downarrow}(0) = 4.84T'_s + 1.78q' + 16.5\tau'_A. \quad (1)$$

where $\hat{R}'_{LW\downarrow}(0)$ is the fitted downward longwave at the surface in W m^{-2} , T'_s is the surface air temperature in K measured by the eddy correlation instrument, q' is the column-integrated water vapor in mm measured by the radiosonde, and τ'_A is the (dimensionless) aerosol optical thickness retrieved from the MFRSR instrument. All

Table 2. Surface Forcing and Response Terms in (2) and Their Correspondence With Measured Variables^a

Symbol	Variable	Measured Quantity
F_{SW}	solar forcing	downwelling minus upwelling shortwave
F_{LW}	longwave forcing	$1.78 q' + 16.5 \tau'_A$
δR_{LW}	net longwave response	upwelling minus downwelling longwave plus F_{LW}
δS_e	sensible heat response	sensible heat flux
$\delta (LE)$	latent heat response	latent heat flux

^aAll quantities are daily averages and anomalies relative to the 2006 calendar year mean. q' is column water vapor from radiosondes; τ'_A is aerosol optical thickness retrieved from MFRSR irradiances.

quantities in (1) correspond to daily averages, and the prime symbol represents an anomaly relative to the 2006 calendar year average.

[33] The measured downward longwave flux at the surface is shown in Figure 6a, along with the fit by the regression model given by (1). In spite of the simplicity of this empirical approach, the regression model accounts for over 97% of the observed variation in the downward longwave flux during 2006. This percentage is stable throughout the year, and falls only to 93% if the regression model is restricted to the dry season (i.e., excluding May through October). While our regression model achieves this good fit without explicitly accounting for variations in clouds, variations in downward longwave due to clouds are implicitly accounted for in the regression model given the 0.41 correlation between water vapor and visible cloud optical thickness retrieved by ISCCP. The variance represented by (1) can be attributed approximately to the individual predictors, given that they are only weakly correlated. Column water vapor (and associated changes in cloud optical thickness) account for nearly two thirds of the downwelling longwave variance, with atmospheric temperature accounting for most of the rest. Aerosols make a dominant contribution to measured longwave fluctuations only episodically, mainly during dust outbreaks.

[34] The dependence of the regression model upon temperature, water vapor, and aerosol is consistent with linearized parameterizations of surface longwave described by *Fung et al.* [1984], where downward longwave into the surface increases with atmospheric emissivity (here represented by aerosol and water vapor) and atmospheric temperature. Because of vertical mixing within the boundary layer during the dry season and within a deeper layer during the summer, the surface air temperature anomaly T'_s is representative of variations in atmospheric temperature within a layer extending well into the troposphere. We construct (1) to distinguish contributions to the measured downwelling longwave by changes in longwave opacity and the atmospheric temperature response. *Slingo et al.* [2009] provide a physical interpretation of atmospheric longwave fluctuations measured during the ARM campaign at Niamey as a result of variations in temperature, moisture, and aerosol using a physically based formula by *Prata* [1996].

[35] In response to a change in atmospheric composition and radiative forcing, the surface energy balance is:

$$\frac{\partial H}{\partial t} = F_{SW} + F_{LW} + \delta R_{LW} + \delta S_e + \delta (LE) \quad (2)$$

Here, H is the heat stored by the surface, and the solar and thermal components of the forcing are F_{SW} and F_{LW} , respectively. The response of the net longwave and turbulent fluxes to the forcing are given by δR_{LW} , δS_e and $\delta (LE)$, respectively, where δS_e is the anomalous sensible heat flux and $\delta (LE)$ is the anomalous latent heat flux.

[36] To calculate the response of the surface fluxes (the terms prefixed by δ) to the forcing, we relate each term on the right side of (2) to a quantity measured at the mobile facility. For the solar forcing F_{SW} , we assign the anomalous net downward flux of solar radiation (Figure 5a). This anomaly is computed by dividing out the slow modulation of the solar flux by the seasonal change in the daily averaged solar zenith angle, using the formula given by *Hartman* [1994, Appendix A], and subtracting the long-term mean. The attribution of the measured solar flux entirely to forcing assumes that shortwave changes in response to the forcing (e.g., through cloud cover) are comparatively small. For the

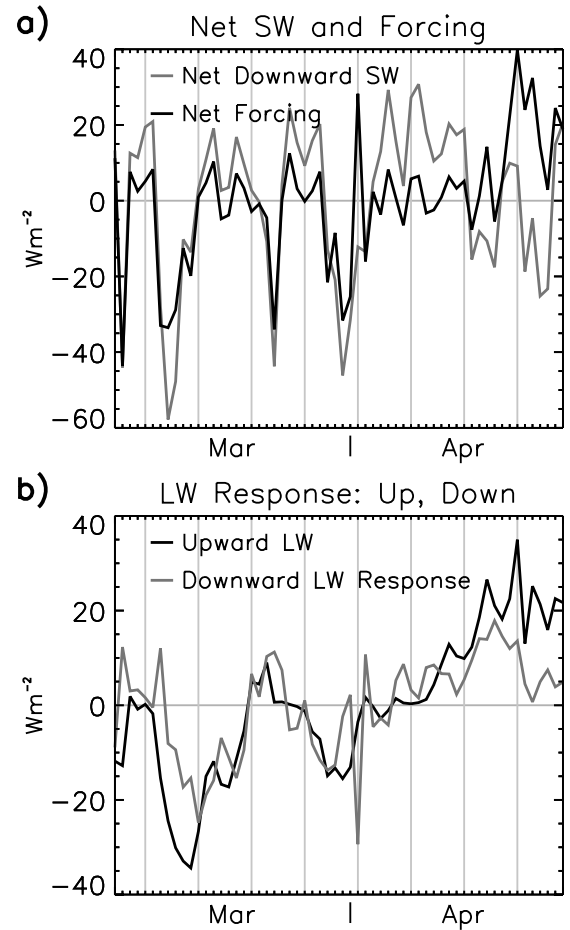


Figure 8. Daily averaged (a) net shortwave (downwelling minus upwelling) along with net forcing equal to net shortwave plus downwelling longwave due to changes in column water vapor and dust aerosol and (b) downwelling longwave associated with changes in atmospheric temperature and upwelling longwave. All quantities are in $W m^{-2}$ and measured (or calculated through regression with measured quantities) during March and April 2006 at the ARM Mobile Facility in Niamey, Niger.

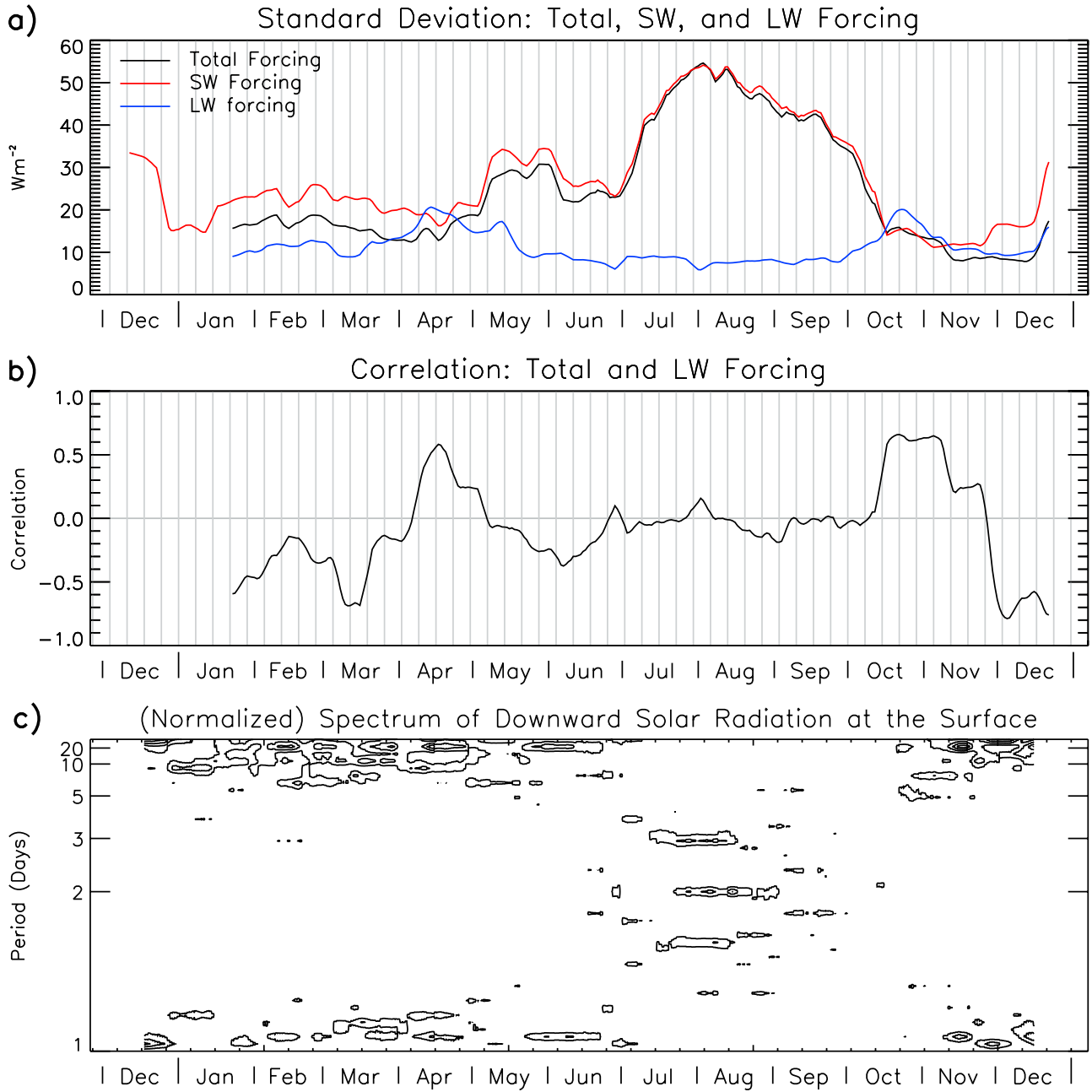


Figure 9. (a) Standard deviation of total along with solar and longwave forcing in $W m^{-2}$ and (b) correlation of total and longwave forcing. The standard deviation and correlation are computed as a function of time within a 29-day window centered at each date. Only correlations with magnitude greater than 0.37 are statistically distinct from zero at the 95% level, according to a two-sided test. (c) Spectrum of downward solar radiation at the surface. The spectrum is computed as a function of time within a 45-day window centered at each date and is normalized to have the same frequency-integrated power at each date. The diurnal cycle within each period is subtracted prior to calculation, although because of slow, seasonal variations in the solar zenith angle within each time window, some diurnal power leaks into periods that are not integer fractions of 1 day, accounting for the quasi-diurnal power at the bottom of Figure 9c.

longwave forcing, F_{LW} , we use the contribution to the observed downward longwave flux by variations in water vapor and aerosol optical thickness, as identified by the regression model (Figure 6b). The time series of the surface net longwave response δR_{LW} is given by the observed upward longwave emission minus the temperature contri-

bution to the observed downward longwave extracted using the regression model. The response of the turbulent fluxes is assumed to be given by the measured fluxes of sensible and latent heat. The forcing and response terms in (2) and their correspondence with measured quantities are summarized in Table 2.

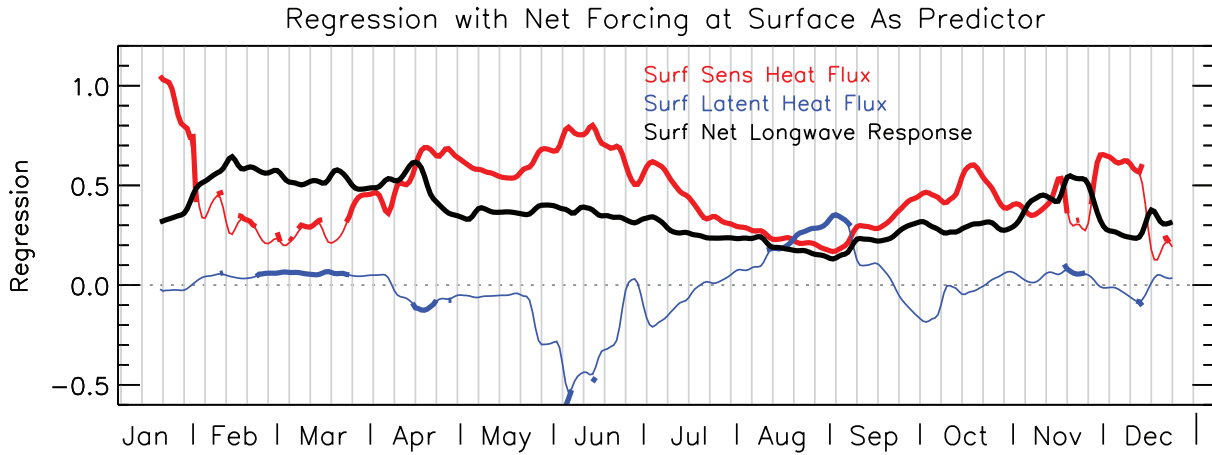


Figure 10. Regression (dimensionless) of the net longwave response and turbulent fluxes with respect to the net surface forcing over the ARM Mobile Facility at Niamey, Niger. For each date, the regression is calculated using measurements ranging from 2 weeks prior to 2 weeks after. A bold line indicates that the regression is statistically distinct from zero at the 95% level, according to a two-sided test. To emphasize seasonal variations, a 1-2-1 smoother is applied twice to the daily regression coefficients (similar to a 5-day running mean).

[37] The net surface forcing and response component of the downward longwave flux are illustrated in Figure 8 during March and April 2006 at the end of the dry season. The net shortwave anomaly due to changes in clouds, column water vapor, and aerosols is offset by longwave emission from these constituents (Figure 8a). Three dust outbreaks can be seen as large reductions in the solar flux during March. The increased downwelling longwave is generally smaller in magnitude than the solar reduction, so that the total forcing has the sign of the solar flux but is smaller in magnitude. During the first dust outbreak in March, both the ground and air temperature are reduced by the passage of a cold front [Slingo *et al.*, 2006], which diminishes both the upwelling longwave measured at the surface and the component of downwelling longwave identified by (1) related to atmospheric temperature (Figure 8b). Two smaller dust events in late April, evident in the net downward solar in Figure 8a, are coincident with a rapid increase in column water vapor associated with the temporary onset of the southwesterly surface wind (Figure 3) [Slingo *et al.*, 2008]. During this time, elevated concentrations of dust and water vapor increase longwave emissivity, resulting in positive total forcing, while warming the surface air and ground, as can be inferred from Figure 8b.

[38] The magnitude and characteristic time scale of variations in net surface forcing are shown in Figure 9. During the dry season, longwave forcing generally offsets the solar contribution to the total but is smaller (Figures 8a and 9a). At the height of the rainy season between July and September, the total forcing is dominated by the solar component, and uncorrelated with variations in longwave forcing (Figure 9b). According to Figure 6b, the small longwave forcing during the rainy season is mainly the result of reduced variations in column water vapor. The marked increase in the variability of the total and solar forcing during the rainy season is related to the passage of African easterly waves [e.g., Burpee, 1972]. This is indicated by the characteristic synoptic time scale in the spectrum of the solar forcing during this season (Figure 9c). The spectrum is computed within a

45-day window centered at each date. To emphasize frequencies longer than a day, the solar time series is filtered to remove frequencies shorter than 12 h, and then subsampled every 6 h to reduce aliasing. We also remove the mean diurnal cycle within each time window. The total spectral power is then normalized to be identical at each date to show how the dominant period (rather than the magnitude of variability) changes over time. Within the dry season, the spectrum is red, with the greatest power at longer periods. However, within the rainy season, periods of a few days dominate, representing synoptic variations in cloud cover associated with African waves modulated by the diurnal cycle of incident sunlight.

4.2. Surface Response to Subseasonal Forcing

[39] How the surface responds to subseasonal variations in surface net radiative forcing is shown in Figure 10. To calculate the response of the surface fluxes, we regress the surface net longwave response along with both the turbulent sensible and latent heat fluxes (each of the terms in equation (2) prefixed by δ) with the surface net forcing (represented by the sum $F_{SW} + F_{LW}$) as a predictor. To show how the response evolves throughout the year, the regression is computed within a 4-week period centered at each date. The 4-week window is chosen to balance the competing need for high time resolution and small sampling uncertainty. The largest regression coefficient on any date shows the predominate mechanism by which the forcing is balanced. The regression coefficients sum to unity when the forcing is completely compensated by these fluxes (rather than being stored as heat within the ground).

[40] During the dry season, net longwave emission and the turbulent flux of sensible heat alternate as the dominant response to subseasonal variations in forcing (Figure 10). Following the arrival of the southwesterly winds in mid-April and the large increase in column water vapor and atmospheric longwave opacity, the ability of the net longwave response to regulate surface temperature decreases. The sensible heat flux increases in response, while the

evaporative response remains low. Only at the height of the rainy season during August and September does evaporative cooling become comparably efficient, when all three fluxes respond to the forcing with nearly equal magnitude.

[41] The dominance of the sensible heat flux in response to surface forcing during the early part of the rainy season, and the comparable importance of the evaporative response at the height of this season can be understood respectively as the result of increased atmospheric longwave opacity and the accumulation of rainfall in the soil that supplies moisture for evaporation. Why the net longwave and sensible heat response alternate in importance during the dry season is less apparent. For example, Figure 10 shows that during January, subseasonal forcing is balanced almost entirely by sensible heating (as indicated by a regression coefficient near unity). However, the efficiency of sensible heating falls off markedly in the following two months when the net longwave response dominates. The net longwave is the difference between the upwelling and downwelling responses, which increase with the ground and air temperature, respectively. Thus, the net longwave response should increase with ground temperature and the ground-air temperature difference.

[42] The sensible heat flux also depends upon the ground-air temperature difference, according to its conventional parameterization [Arya, 2001]:

$$S_e = C_p \rho C_D |w| (T_g - T_s), \quad (3)$$

where C_p is the heat capacity of air at constant pressure, ρ is the air density, C_D is a heat transfer coefficient that is generally parameterized in terms of atmospheric stability, w is the surface wind speed, T_g is the ground temperature, and T_s is the surface air temperature that appears in (1). According to (3), the sensible heat flux varies with the ground-air temperature difference (like the net longwave response), but also with the product $C_p \rho C_D |w|$ that we refer to as a “bulk coefficient,” which is related to mixing within the boundary layer. Thus, a change in boundary layer mixing and the bulk coefficient in response to the forcing will change the importance of the sensible heat response compared to the net longwave. Miller *et al.* [2004a] describe an example of how dust aerosol forcing changes boundary layer mixing in an atmospheric general circulation model (AGCM). Negative aerosol forcing at the surface reduces the sensible heat flux, which powers mixing within dry, continental boundary layers [e.g., Arya, 2001]. A reduction in the vigor of boundary layer mixing results in less momentum transported downward to the surface, reducing the bulk coefficient through its dependence upon the surface wind speed w . (The direct reduction in eddy wind fluctuations associated with decreased mixing causes a similar reduction in wind speed.) This reinforces the original reduction in the surface heat flux, indicating a positive feedback. This feedback has been found in additional models [Pérez *et al.*, 2006; Heinold *et al.*, 2007]. Equation (3) indicates that the bulk coefficient inferred from the AMF measurements might be used to understand the relative efficiency of the longwave and sensible heat response during the dry season.

[43] One caveat should be noted about our decomposition of measured quantities into a forcing and response. We have

attributed any change in atmospheric or ground temperature as a response to forcing. Especially during the dry season, changes in atmospheric constituents like clouds or aerosols may result from the arrival of a cold front extending from higher latitudes [e.g., Slingo *et al.*, 2006]. In this case, the measured temperature change results partly from advection and is not solely the local response to radiative forcing resulting from the change in atmospheric composition. The advective contribution to temperature will project spuriously onto the net longwave efficiency in Figure 10. This introduces an error that is difficult to characterize, but which we have assumed to be small. Similarly, changes to boundary layer dynamics by variations in radiative forcing might be obscured by the frontal circulation that drives the change in atmospheric constituents.

[44] To focus upon the surface response to aerosol radiative forcing (as opposed to forcing by variations in water vapor and clouds), we repeat the regression calculation using the MFRSR AOT as the predictor. We perform the regression for March and April 2006 to see the response to several significant dust events during this period. The surface response is shown in Figure 11. The surface radiative forcing by dust is balanced by roughly equal reductions in the turbulent flux of sensible heat into the atmosphere and the net upward longwave response. The anomalous net upward longwave response is negative because the ground cools more than the atmosphere, as implied by the individual upward and downward longwave responses in Figure 11b. If the period of the regression calculation is extended through the end of June, when the atmospheric longwave opacity has been increased by the arrival of moist monsoonal air, dust radiative forcing is balanced almost entirely by the sensible heat flux.

4.3. Contrasting Evaporative Response to Forcing During the Rainy Season

[45] In contrast to the turbulent flux of sensible heat, the latent heat flux shows almost no variation with forcing throughout the dry season (Figure 10), consistent with the small seasonal average of this flux (Figure 7a). Only at the height of the rainy season in August does evaporation increase to compensate additional sunlight (Figure 10). Earlier in the rainy season, the regression coefficient between the latent heat flux and solar heating is negative: evaporation increases despite a reduction in sunlight. We interpret this anticorrelation as a consequence of limited soil moisture prior to the significant accumulation of seasonal rainfall. The clouds bringing the first rains early in the southwesterly phase of the monsoon reduce the sunlight incident upon the surface. At the same time, the rainwater supplies moisture to the surface that is quickly depleted within a few days by evaporation. Thus, the anticorrelation results from the temporary availability of surface water for evaporation at the same time that the rain clouds shield the surface from sunlight.

[46] Figure 12 shows evaporation as a function of precipitation, where evaporation is computed as an anomaly relative to its average over the 5 days prior to the rain event. That is, the plot shows how evaporation is changed by the occurrence of rainfall. To see the effect of soil moisture accumulating over the course of the season, we distinguished between the periods before and after July 15, which

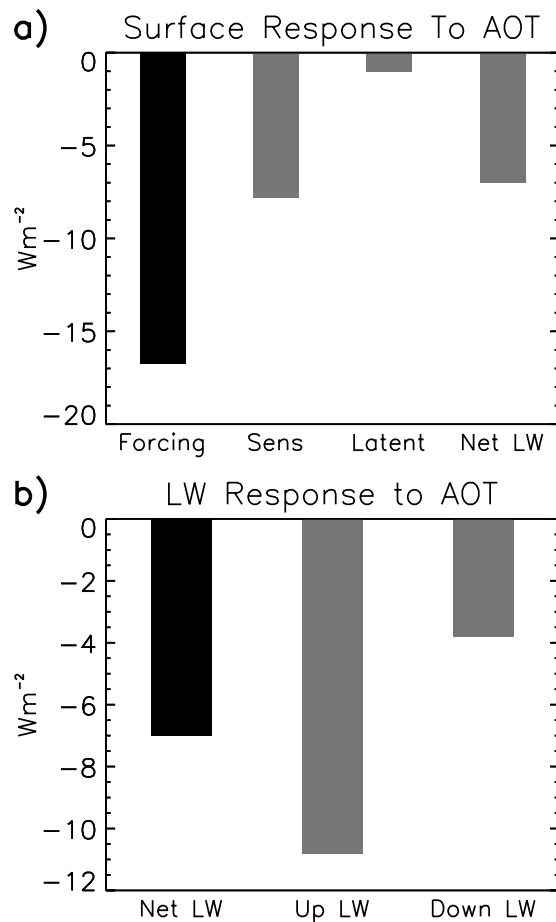


Figure 11. Regression of surface fluxes with respect to MFRSR AOT measured at the ARM Mobile Facility at Niamey, Niger. The regression is calculated using measurements during March and April 2006, when there were several large dust events. The standard deviation of AOT during this period is 0.46. The mean diurnal cycle is subtracted prior to calculation of the covariance. Regression of AOT versus (a) dust radiative forcing at the surface, along with the turbulent fluxes and net longwave response, and (b) individual components of the net longwave response: the upward longwave flux and the contribution of downward longwave related to atmospheric temperature.

during 2006 was roughly the date when precipitation became more frequent, and accumulated rainfall started to increase most rapidly. For the earlier period, the evaporative anomalies (plotted in red) are with one exception positive.

[47] In contrast, the average evaporative anomaly is zero following precipitation during the second part of the rainy season (plotted in blue). The range of values for the two periods (given by the vertical black lines, which span one standard deviation above and below the mean) are not statistically distinct. Nonetheless, evaporation decreases in response to rain almost as often as it increases during the second period. This suggests that the reservoir of soil moisture has sufficiently refilled such that evaporation is no longer tied to moisture delivery by a recent rain event. Solar heating of the surface has replaced the availability of water as the factor controlling evaporation, and the latent heat flux can buffer the surface from variations in sunlight,

as indicated by the positive correlation between the surface net forcing and evaporation (Figure 10). Note that the regression between the solar flux and evaporation switches sign from negative to positive around the middle of July (Figure 10), during a sustained increase of the cumulative precipitation (Figure 2a).

[48] The temporary increase in evaporation following an early season rain event, as observed at the AMF during the first half of the rainy season (Figure 12, red), was also noted during HAPEX-Sahel [Gash *et al.*, 1997]. This and other studies show that this temporary increase is related to increased evaporation from the unvegetated soil fraction at the expense of transpiration by the vegetation [Wallace *et al.*, 1993; Allen and Grime, 1995]. The partitioning between soil evaporation and transpiration depends upon the plant species and soil type. For example, where the soil surface inhibits the penetration of rainwater, soil evaporation may increase after a storm at the expense of moisture storage within the soil and subsequent transpiration. The decoupling of evaporation and precipitation at the AMF during the latter half of the rainy season (Figure 12, blue) suggests that rainwater is able to penetrate the soil, creating a reservoir that eventually allows evaporation to respond to subsequent variations in solar heating of the surface. In contrast, Gash *et al.* [1997] found that evaporation and rainfall were coupled as late in the rainy season as September, rather than decorrelating with the accumulation of sufficient precipitation as at the AMF. This may reflect differences in the soil and vegetation at the HAPEX-Sahel and AMF sites. The history of rainfall and its accumulation during a particular season are also an important control upon the coupling between precipitation and evaporation.

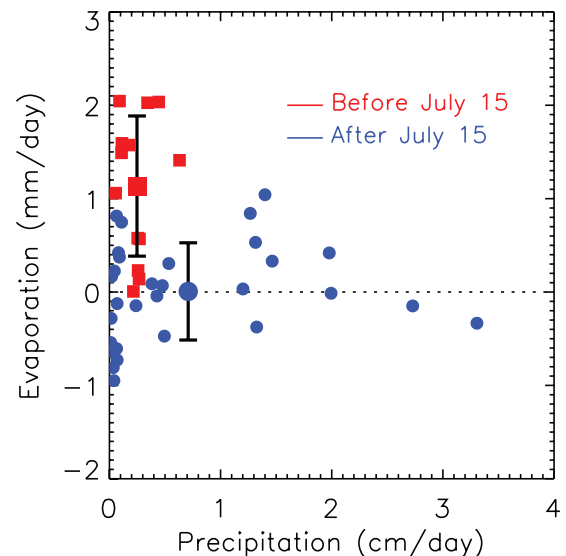


Figure 12. Relation between daily averaged precipitation and anomalous evaporation measured at the AMF in Niamey. Red squares signify rain events during the period before 15 July 2006; blue circles signify events after this date. The mean is indicated by a larger symbol, with a black line extending one standard deviation above and below. Evaporation anomalies are computed relative to an average over the preceding 5 days.

[49] During 2006, there was little additional rainfall after mid-September (Figure 2a). By November, the latent heat flux returned to near zero, indicating that the moisture accumulated within the soil during the rainy season was no longer available for evaporation. This may indicate a depletion of the reservoir, or the absence by this time of vegetation to draw moisture to the surface (Figure 2b).

5. Implications for Seasonal Forecasting and Projections of Twenty-First Century Climate

[50] Sahel precipitation is distinguished by large year-to-year persistence and decadal variability compared to rainfall variations along the Guinea coast and throughout southern Africa, where interannual fluctuations are more prominent [Nicholson and Entekhabi, 1986]. This persistence within the Sahel suggests the potential for seasonal forecasts of summer precipitation. Some predictions have been based upon ocean temperatures anomalies [Folland *et al.*, 1991]. In addition, Koster *et al.* [2004] show that in certain climate models, soil moisture prescribed within the Sahel at the beginning of June influences simulated precipitation during the subsequent summer months. A predictive role for soil moisture is also suggested by observations showing that almost half of summertime rainfall within the Sahel originates as local evaporation [Brubaker *et al.*, 1993].

[51] While soil moisture influences rainfall in AGCMs, evaporation measured at the AMF during 2006 remained virtually zero for a month after the arrival of the moist southwesterly winds, and increased only after the first significant precipitation (Figure 2a). This suggests either that there was no soil moisture to evaporate, despite unusually large rainfall during the year prior to the AMF measurement campaign [Slingo *et al.*, 2008], or that any stored moisture can be accessed only after vegetation extends its roots beneath the surface. At the AMF, evaporation increased concurrently with the leaf area index (Figure 2b). This concurrence may simply indicate that the growth of vegetation follows the regular occurrence of rainfall, which also supplies moisture for evaporation. However, previous field measurements have shown that a significant fraction of total evaporation is supplied through transpiration [e.g., Gash *et al.*, 1997], and the concurrence may indicate that vegetation taps moisture from beneath the surface that otherwise would have remained in storage. This opens the possibility that certain plants extend their roots deep enough to tap moisture accumulated during a prior year. At the AMF, measured evaporation and leaf area index were largest during August and September, when the persistence of rainfall anomalies from one year to the next is largest [Nicholson and Palao, 1993]. The covariability of evaporation and vegetation measured by the AMF is consistent with the suggestion that moisture storage increases the persistence of multiyear rainfall anomalies [Nicholson, 2000]. This covariability also suggests that seasonal forecasts of rainfall based upon initial knowledge of soil moisture will require an accurate representation of vegetation and its ability to tap moisture for transpiration.

[52] Climate models have been used to assess the possibility of forecasting Sahel precipitation [e.g., Koster *et al.*, 2004], but simulation of the seasonal cycle of Sahel climate remains a challenge for many models. Among the coupled

model simulations of twentieth-century climate submitted to the Fourth Assessment Report of the Intergovernmental Panel on Climate Change, almost half placed the maximum in summertime precipitation over the equatorial Atlantic, as opposed to the observed location over the West African continent. Moreover, there is wide disagreement of even the sign of the projected anomaly of Sahel rainfall during the twenty-first century [Biasutti *et al.*, 2008].

[53] The AMF measurements of the surface energy balance offer a number of constraints that should be used to test and improve models. One key measurement for a model to reproduce is the seasonal contrast of the surface net long-wave flux, which indicates the reversal of the monsoon circulation and the arrival of moist air within the Sahel that is relatively opaque to longwave radiation. The observed seasonal dependence of evaporation measures the fidelity of model precipitation and the land surface scheme. Evaporation is small throughout the dry season and immediately following the springtime reversal of the monsoon winds. Rather than buffer the surface temperature against solar heating at the start of the rainy season, model evaporation should initially reinforce the cooling of the surface that results from an increase in precipitating cloud cover. Only as the reservoir of soil moisture refills throughout the rainy season should evaporation begin to increase with incident sunlight. During the dry season, when evaporation is small, the measured partitioning between the upward longwave and sensible heat flux is a test of heat transport within the model's boundary layer.

[54] While the AMF instruments are located within a savanna, many of these tests of model behavior follow from the negligible evaporation outside the height of the rainy season, which has been found during measurement campaigns like SEBEX and HAPEX-Sahel over a range of surface and vegetation types. The ability of a climate model to simulate these robust features of the AMF surface flux measurements reflects upon the model simulation of many broader aspects of the West African monsoon, including the strength and timing of the monsoon circulation, storage of moisture beneath the land surface, the flux of moisture by transpiration and soil evaporation to feed rainfall, and the mixing of heat and moisture across the boundary layer.

6. Conclusions

[55] We have described monsoonal variations in the surface energy balance at a site within the Sahel, using measurements of radiative and turbulent fluxes at the ARM Mobile Facility stationed at Niamey, Niger throughout 2006. The AMF was situated within the Sahel as part of the RADAGAST experiment that was designed to measure surface fluxes in conjunction with retrievals of TOA radiation by the GERB instrument on Meteosat-8, with the ultimate goal of observing atmospheric radiative divergence [Slingo *et al.*, 2009]. The instruments were located within a savanna, with rainfall restricted to the southwesterly phase of the West African Monsoon, when surface winds bring moist air from the tropical Atlantic Ocean. The phase of the monsoon wind determines how solar heating is balanced by the land surface at Niamey. During the dry season, solar heating is balanced predominately by longwave radiation and the turbulent flux of sensible heat. Only at the height of

the rainy season is evaporation of comparable importance in balancing sunlight.

[56] This seasonal contrast is attributed to two factors. First, soil moisture is available for evaporation only after the return of regular precipitation, in contrast to the ocean or more vegetated regions where evapotranspiration can supply moisture to the atmosphere throughout the year. Early in the rainy season, evaporation increases temporarily following the occurrence of precipitation and is negatively correlated with the reduction in solar heating beneath precipitating clouds. Sufficient accumulation of soil moisture by the height of the rainy season allows evaporation to decorrelate with the supply of water from recent precipitation events, and correlate positively with the flux demanded by solar heating of the surface.

[57] As a consequence of the restriction of significant evaporation to the height of the rainy season at Niamey, dimming of the surface by aerosols weakens the hydrologic cycle only during this period [Miller and Tegen, 1998; Ramanathan et al., 2001], and the hydrologic cycle is decorrelated from local aerosol forcing at other times of the year.

[58] The sharp seasonal contrast in the surface energy balance is also related to the annual change in longwave opacity associated with the seasonal reversal of wind direction associated with the monsoon. With the arrival of relatively cool, moist air from the Atlantic Ocean during late April, the column moisture increases threefold. This moisture increases the atmospheric absorption of longwave radiation emitted by the surface, redirecting more of it downward, reducing the ability of the surface to cool through longwave radiation. In contrast, during the dry season between November and April, the mean winds are from the Sahara desert to the north and the column is relatively transparent in the longwave, allowing the surface to cool efficiently by radiating directly to space.

[59] In general, how the surface balances solar heating varies with seasonal changes in atmospheric water vapor, which modulates the greenhouse effect and the ability of the surface to radiate thermal energy directly to space. Radiative forcing of the surface also results from more rapid, sub-seasonal variations in atmospheric constituents like water vapor, clouds, and aerosols. On these shorter time scales, the net longwave response and the turbulent flux of sensible heat alternate in their ability to regulate the surface temperature, except at the height of the rainy season when evaporation has a comparable effect. It is not understood under what conditions the sensible heat flux should dominate the longwave response to subseasonal forcing during the dry season, but we believe this is an interesting question, especially when the forcing results from a dust aerosol outbreak. A reduction in the sensible heat flux affects boundary layer mixing and the surface wind speed that raises dust into the atmosphere in the first place. We have also noted the possibility for boundary layer mixing to amplify the sensible heat response. We suggest that the response of the boundary layer to surface radiative forcing be investigated with the AMF measurements to understand when the sensible heat response will dominate the net longwave.

[60] The concurrence of the seasonal cycles of evaporation and the leaf area index at the AMF may simply indicate that both increase in response to rainfall. However, this

concurrence is also consistent with previous measurements showing that transpiration is an important component of the total evaporation [e.g., Gash et al., 1997]. The ability of plant roots to tap moisture below the soil surface may provide access to moisture stored during a previous rainy season, linking rainfall in successive years and offering the possibility of seasonal forecasts based upon knowledge of soil moisture. The latter months of the rainy season, when vegetation is most extensive, is also the period when the year-to-year persistence of rainfall anomalies is greatest [Nicholson and Palao, 1993]. Successful seasonal forecasts based upon initial knowledge of soil moisture must accurately represent the emergence of vegetation and its transfer of subsurface moisture to the atmosphere.

[61] While the mobile facility at Niamey provides detailed measurements at a single site, the meteorological and radiative properties that were observed reflect regional aspects of the West African monsoon, such as its timing and delivery of moisture. As such, the measurements at the AMF during RADAGAST are a valuable test of climate models and their simulation of the monsoon circulation.

Appendix A

[62] In this appendix, we show that the overlap of rainy days identified by the ARM Mobile Facility optical instrument and the operational rain gauge is unlikely to result from chance, indicating that both instruments have skill at detecting the occurrence of rainfall, despite any disagreement over the amount. The appendix is intended to document the performance of the optical instrument, and may be skipped by readers interested in the climate implications of the measurements.

[63] By analogy, consider N distinct items and select n of them. After replacement, select m items and calculate the probability that k were selected both times. Here N could represent the total number of days during the rainy season, while n and m are the number of rainy days identified by the airport rain gauge and the AMF optical instrument, respectively. We want to know if the k rainy days in common between the two instruments are likely to result merely from random chance, indicating that one or both of the instruments has no skill at detecting rainfall.

[64] The probability that the first item selected in the second round was also chosen in the first round is $\frac{n}{N}$. Similarly, the probability that the first two items of the second round were selected in the first round is $\frac{n}{N} \frac{n-1}{N-1}$. In general, the probability $p_{k,m-k}$ that the first k items in the second round were chosen in the first round, while the subsequent $m-k$ items were not is:

$$p_{k,m-k}(N, n, m, k) = \left(\frac{n}{N}\right) \left(\frac{n-1}{N-1}\right) \cdots \left(\frac{n-k+1}{N-k+1}\right) \cdot \left(\frac{N-n}{N-k}\right) \left(\frac{N-n-1}{N-k-1}\right) \cdots \left(\frac{N-n-(m-k)+1}{N-m+1}\right). \quad (\text{A1})$$

The first row of (A1) gives the probability of the first k items from the second round being in common with those chosen during the first. The second row gives the probability of the remaining $m-k$ items being unique to

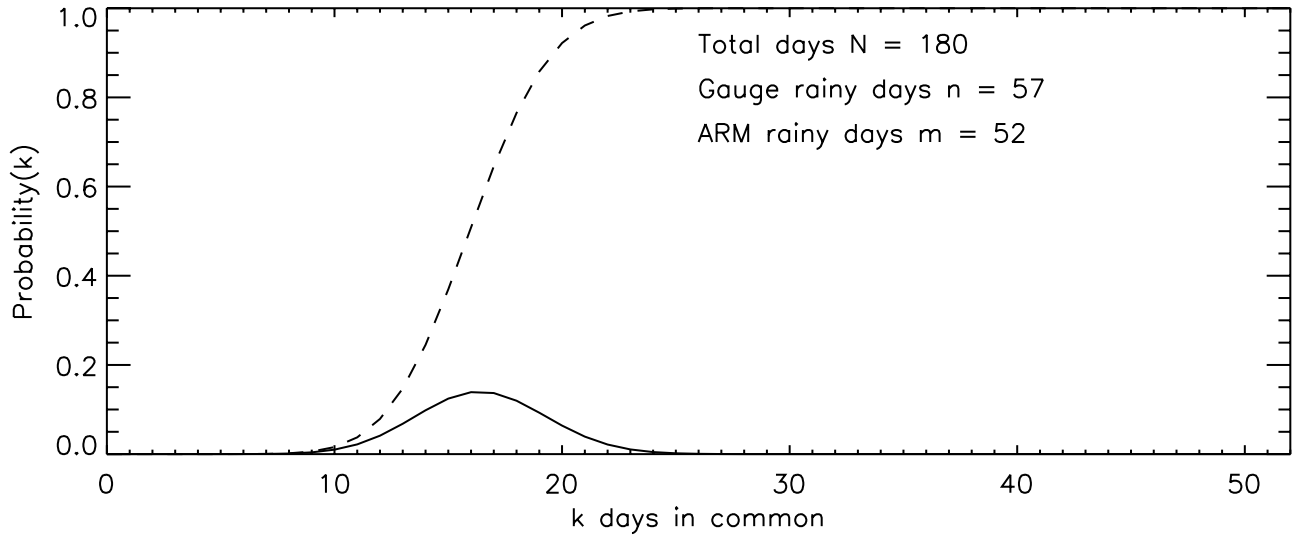


Figure A1. Probability (solid) of the 57 rainy days identified by the airport rain gauge and the 52 days identified by the AMF optical instrument having k days in common if one or both instruments have no skill in identifying rainy days. The dashed line shows the cumulative probability that the two data sets have less than k days in common.

the second round. If the k repeated and $m-k$ new items were chosen during the second round in a different order, then the numerators and denominators in (A1) would simply be rearranged, so that the sequence would have the same probability $p_{k,m-k}(N, n, m, k)$. There are $\binom{m}{k}$ ways in which the k common days can be selected among the total m during the second round, and each has equal probability. (Here, $\binom{m}{k}$ has the conventional definition of $\frac{m!}{k!(m-k)!}$.) Thus, the total probability of selecting k days in common is:

$$p(N, n, m, k) = \binom{m}{k} p_{k,m-k}(N, n, m, k) \quad (\text{A2})$$

which we can rewrite as:

$$\begin{aligned} p(N, n, m, k) &= \frac{m! (N-n)! (N-m)!}{k! (m-k)! (n-k)! (N+k-m-n)! N!} \\ &= \binom{n}{k} \binom{N-n}{m-k} / \binom{N}{m}. \end{aligned} \quad (\text{A3})$$

Note that the probability is the same when n and m are reversed, as expected by symmetry. Also, by applying Vandermonde's identity [e.g., Freund, 1992, theorem 1.12], it can be shown that

$$\sum_{k=0}^m p(N, n, m, k) = 1. \quad (\text{A4})$$

[65] Setting N equal to 180 (roughly the number of days in the rainy season), with n and m equal to 57 and 52 as identified by the airport rain gauge and optical instrument, then random chance would result in between 9 and 24 common days 99% of the time (Figure A1). In fact, the two

instruments have 39 days in common and as many as 45 if storms around midnight assigned to successive days by the two instruments are included. According to Figure A1, this overlap is very unlikely, and suggests that despite the deposition of dust aerosols on the optical instrument, it remained sensitive to the occurrence of rain.

[66] **Acknowledgments.** Data were obtained from the Atmospheric Radiation Measurement (ARM) Program sponsored by the U.S. Department of Energy, Office of Science, Office of Biological and Environmental Research, Environmental Sciences Division. The article was improved by the comments of three anonymous reviewers. We also thank Nazim Bharmal, Chris Bishop, Brian Cairns, Anthony Del Genio, Hamidou Hama, Kenneth Kehoe, Randall Koster, Peter Lamb, Issa Lélé, Sally McFarlane, Mark Miller, Sharon Nicholson, Randy Peppler, Michael Puma, Chris Taylor, Dave Turner, Peng Xian, and Wenze Yang for their comments and advice. In addition, we thank Didier Tanré for aerosol retrievals from the AERONET site at Banizoumbou, Niger, and the Boston University Group for their MODIS vegetation products. This work was supported by the Climate Dynamics Program of the National Science Foundation through ATM-06-20066. A.S. was supported by the United Kingdom Natural Environment Research Council. The Pacific Northwest National Laboratory is operated by Battelle Memorial Institute, Pacific Northwest Division, for the U.S. Department of Energy (DOE). This research was supported in part by the DOE office of Biological and Environmental Research through the Atmospheric Radiation Measurement (ARM) program under contract DE-AC05-76RL01830 to the Pacific Northwest National Laboratory. This article is dedicated to the memory of Christopher Bishop and Anthony Slingo.

References

- Allen, S. J., and V. Grime (1995), Measurements of transpiration from savannah shrubs using sap flow gauges, *Agric. For. Meteorol.*, 75, 23–41.
- Arya, S. P. (2001), Introduction to Micrometeorology, *Int. Geophys. Ser.*, vol. 79, 450 pp., Academic, San Diego, Calif.
- Bharmal, N. A., A. Slingo, G. J. Robinson, and J. J. Settle (2009), Simulation of surface and top of atmosphere thermal fluxes and radiances from the RADAGAST experiment, *J. Geophys. Res.*, doi:10.1029/2008JD010504, in press.
- Biasutti, M., I. M. Held, A. H. Sobel, and A. Giannini (2008), SST forcings and Sahel rainfall variability in simulations of the twentieth and twenty-first centuries, *J. Clim.*, 21(14), 3471–3486, doi:10.1175/2007JCLI1896.1.
- Bock, O., et al. (2008), West African Monsoon observed with ground-based GPS receivers during African Monsoon Multidisciplinary Analysis (AMMA), *J. Geophys. Res.*, 113, D21105, doi:10.1029/2008JD010327.

- Brubaker, K. L., D. Entekhabi, and P. Eagleson (1993), Estimation of continental precipitation recycling, *J. Clim.*, **6**, 1077–1089, doi:10.1175/1520-0442(1993)006<1077:EOCPR>2.0.CO;2.
- Burpee, R. W. (1972), The origin and structure of easterly waves in the lower troposphere of North Africa, *J. Atmos. Sci.*, **29**, 77–90.
- Claquin, T., M. Schulz, Y. Balkanski, and O. Boucher (1998), Uncertainties in assessing radiative forcing by mineral dust, *Tellus, Ser. B*, **50**, 491–505.
- Coakley, J. A., and R. D. Cess (1985), Response of the NCAR Community Climate Model to the radiative forcing by the naturally occurring tropospheric aerosol, *J. Atmos. Sci.*, **42**, 1677–1692.
- Cook, D. R., and M. S. Pekour (2008), Eddy correlation flux measurement system handbook, *Tech. Rep. DOE/SC-ARM/TR-05*, Off. of Biol. and Environ. Res., Off. of Sci., U. S. Dep. of Energy, Washington, D. C.
- Emanuel, K. A. (1994), *Atmospheric Convection*, 580 pp., Oxford Univ. Press, Oxford, U. K.
- Folland, C., J. Owen, M. N. Ward, and A. Colman (1991), Prediction of seasonal rainfall in the Sahel region using empirical and dynamical methods, *J. Forecast.*, **10**, 21–56, doi:10.1002/for.3980100104.
- Fouquart, Y., B. Bonnell, G. Brogniez, J. C. Buriez, L. Smith, J. J. Morcrette, and A. Cerf (1987a), Observations of Saharan aerosols: Results of ECLATS field experiment. Part II: Broadband radiative characteristics of the aerosols and vertical radiative flux divergence, *J. Appl. Meteorol.*, **26**, 38–52.
- Fouquart, Y., B. Bonnell, M. C. Roquai, and R. Santer (1987b), Observations of Saharan aerosols: Results of ECLATS field experiment. Part I: Optical thicknesses and aerosol size distributions, *J. Appl. Meteorol.*, **26**, 28–37.
- Frangi, J. P., A. Druilhet, P. Durand, H. Ide, J. P. Pages, and A. Tinga (1992), Energy budget of the Sahelian surface-layer, *Ann. Geophys.*, **10**, 25–33.
- Freund, J. E. (1992), *Mathematical Statistics*, 5th ed., 658 pp., Prentice-Hall, Englewood Cliffs, N. J.
- Fung, I. Y., D. E. Harrison, and A. A. Lacis (1984), On the variability of the net longwave radiation at the ocean surface, *Rev. Geophys.*, **22**, 177–193.
- Gash, J., J. Wallace, C. Lloyd, A. Dolman, M. Sivakumar, and C. Renard (1991), Measurements of evaporation from fallow Sahelian Savannah at the start of the dry season, *Q. J. R. Meteorol. Soc.*, **117**, 749–760.
- Gash, J., et al. (1997), The variability of evaporation during the HAPEX-Sahel Intensive Observation Period, *J. Hydrol.*, **188**–189, 385–399.
- Guedalia, D., C. Estournel, and R. Vehil (1984), Effects of Sahel dust layers upon nocturnal cooling of the atmosphere (ECLATS experiment), *J. Appl. Meteorol.*, **23**, 644–650.
- Harrison, L., J. Michalsky, and J. Berndt (1994), Automated multifilter rotating shadow-band radiometer: An instrument for optical depth and radiation measurements, *Appl. Opt.*, **33**, 5118–5125.
- Hartman, D. L. (1994), *Global Physical Climatology*, 411 pp., Academic, New York.
- Heinold, B., J. Helmet, O. Hellmuth, R. Wolke, A. Ansmann, B. Martcorena, B. Laurent, and I. Tegen (2007), Regional modeling of Saharan dust events using LM-MUSCAT: Model description and case studies, *J. Geophys. Res.*, **112**, D11204, doi:10.1029/2006JD007443.
- Huffman, G., R. Adler, P. Arkin, A. Chang, R. Ferraro, A. Gruber, J. Janowiak, A. McNab, B. Rudolph, and U. Schneider (1997), The Global Precipitation Climatology Project (GPCP) combined precipitation dataset, *Bull. Am. Meteorol. Soc.*, **78**, 5–20.
- Johnson, B. T., B. Heese, S. A. McFarlane, P. Chazette, A. Jones, and N. Bellouin (2008), Vertical distribution and radiative effects of mineral dust and biomass burning aerosol over West Africa during DABEX, *J. Geophys. Res.*, **113**, D00C12, doi:10.1029/2008JD009848.
- Kiehl, J. T., and K. E. Trenberth (1997), Earth's annual global mean energy budget, *Bull. Am. Meteorol. Soc.*, **78**, 197–208.
- Koster, R. D., et al. (2004), Regions of strong coupling between soil moisture and precipitation, *Science*, **305**, 1138–1140, doi:10.1126/science.1100217.
- Liu, W. T., A. Zhang, and J. K. B. Bishop (1994), Evaporation and solar irradiance as regulators of sea surface temperature in annual and inter-annual changes, *J. Geophys. Res.*, **99**(C6), 12,623–12,638.
- McFarlane, S. A., E. Kassianov, J. Barnard, C. Flynn, and T. P. Ackerman (2009), Surface shortwave aerosol radiative forcing during the Atmospheric Radiation Measurement Mobile Facility deployment in Niamey, Niger, *J. Geophys. Res.*, doi:10.1029/2008JD010491, in press.
- Miller, M. A., and A. Slingo (2007), The Arm Mobile Facility and its first international deployment: Measuring radiative flux divergence in West Africa, *Bull. Am. Meteorol. Soc.*, **88**(8), 1229–1244, doi:10.1175/BAMS-88-8-1229.
- Miller, R. L., and I. Tegen (1998), Climate response to soil dust aerosols, *J. Clim.*, **11**, 3247–3267.
- Miller, R. L., J. Perlwitz, and I. Tegen (2004a), Feedback by dust radiative forcing upon dust emission through the planetary boundary layer, *J. Geophys. Res.*, **109**, D24209, doi:10.1029/2004JD004912.
- Miller, R. L., I. Tegen, and J. Perlwitz (2004b), Surface radiative forcing by soil dust aerosols and the hydrologic cycle, *J. Geophys. Res.*, **109**, D04203, doi:10.1029/2003JD004085.
- Nicholson, S. (2000), Land surface processes and Sahel climate, *Rev. Geophys.*, **38**, 117–139.
- Nicholson, S. E., and D. Entekhabi (1986), The quasi-periodic behavior of rainfall variability in Africa and its relation to the Southern Oscillation, *Arch. Meteorol. Geophys. Bioklimatol., Ser. A*, **34**, 311–348.
- Nicholson, S. E., and J. P. Grist (2003), The seasonal evolution of the atmospheric circulation over West Africa and equatorial Africa, *J. Clim.*, **16**, 1013–1030.
- Nicholson, S., and I. Palao (1993), A re-evaluation of rainfall variability in the Sahel. Part I. Characteristics of rainfall fluctuations, *Int. J. Climatol.*, **13**, 371–389.
- Pagès, J. P., J.-P. Frangi, P. Durand, C. Estournel, and A. Druilhet (1988), Etude de la couche limite de surface Sahélienne-Experience yantala, *Boundary Layer Meteorol.*, **43**, 183–203.
- Pérez, C., S. Nickovic, G. Pejanovic, J. M. Baldasano, and E. Özsoy (2006), Interactive dust-radiation modeling: A step to improve weather forecasts, *J. Geophys. Res.*, **111**, D16206, doi:10.1029/2005JD006717.
- Prata, A. J. (1996), A new long-wave formula for estimating downward clear-sky radiation at the surface, *Q. J. R. Meteorol. Soc.*, **122**, 1127–1151, doi:10.1256/smsqj.53305.
- Ramage, C. S. (1971), *Monsoon Meteorology*, 296 pp., Academic, New York.
- Ramanathan, V., R. D. Cess, E. F. Harrison, P. Minnis, B. R. Barkstrom, E. Ahmad, and D. L. Hartmann (1989), Cloud-radiative forcing and climate: Results from the Earth Radiation Budget Experiment, *Science*, **243**, 57–63.
- Ramanathan, V., P. J. Crutzen, J. T. Kiehl, and D. Rosenfeld (2001), Aerosols, climate, and the hydrologic cycle, *Science*, **294**, 2119–2124.
- Randel, D. L., T. J. Greenwald, T. H. V. Haar, G. L. Stephens, M. A. Ringerud, and C. L. Combs (1996), A new global water vapor dataset, *Bull. Am. Meteorol. Soc.*, **77**, 1233–1246, doi:10.1175/1520-0477(1996)077<1233:ANGWVD>2.0.CO;2.
- Raval, A., and V. Ramanathan (1989), Observational determination of the greenhouse effect, *Nature*, **342**, 758–761.
- Rosow, W., and E. Duenas (2004), The International Satellite Cloud Climatology Project (ISCCP) web site: An online resource for research, *Bull. Am. Meteorol. Soc.*, **85**, 167–172, doi:10.1175/BAMS-85-2-167.
- Simpson, J. J., J. S. Berg, C. J. Koblinsky, G. L. Hufford, and B. Beckley (2001), The NVAP global water vapor dataset: Independent cross-comparison and multiyear variability, *Remote Sens. Environ.*, **76**, 112–129.
- Slingo, A., et al. (2006), Observations of the impact of a major Saharan dust storm on the atmospheric radiation balance, *Geophys. Res. Lett.*, **33**, L24817, doi:10.1029/2006GL027869.
- Slingo, A., et al. (2008), Overview of observations from the RADAGAST experiment in Niamey, Niger: Meteorology and thermodynamic variables, *J. Geophys. Res.*, **113**, D00E01, doi:10.1029/2008JD009909.
- Slingo, A., H. E. White, N. A. Bharnal, and G. J. Robinson (2009), Overview of observations from the RADAGAST experiment in Niamey, Niger: 2. Radiative fluxes and divergences, *J. Geophys. Res.*, **114**, D00E04, doi:10.1029/2008JD010497.
- Verhoef, A., S. J. Allen, and C. R. Lloyd (1999), Seasonal variation of surface energy balance over two Sahelian surfaces, *Int. J. Climatol.*, **19**, 1267–1277.
- Wallace, J., C. R. Lloyd, and M. V. K. Sivakumar (1993), Measurement of soil, plant and total evaporation from millet in Niger, *Agric. For. Meteorol.*, **63**, 149–169.
- Webster, P. J. (1987), The elementary monsoon, in *Monsoons*, edited by J. Fein and P. Stephens, pp. 3–32, John Wiley, New York.
- Yang, W., D. Huang, B. Tan, J. C. Stroeve, N. V. Shabanov, Y. Knyazikhin, R. R. Nemani, and R. B. Myneni (2006a), Analysis of leaf area index and fraction of PAR absorbed by vegetation products from the Terra MODIS sensor: 2000–2005, *IEEE Trans. Geosci. Remote Sens.*, **44**(7), 1829–1841.
- Yang, W., et al. (2006b), MODIS leaf area index products: From validation to algorithm improvement, *IEEE Trans. Geosci. Remote Sens.*, **44**, 1885–1896.

J. C. Barnard and E. Kassianov, Pacific Northwest National Laboratory, Richland, WA 99352, USA.

R. L. Miller, NASA Goddard Institute for Space Studies, 2880 Broadway, New York, NY 10025, USA. (rmiller@giss.nasa.gov)